

Numerical investigation of the wavy channel geometry and its effect on heat transfer performance in natural convection flow

Andreas Stengaard Thorstensen and Bjørn Christian Dueholm

Energy Technology, TEPE4-1000, 2020-06

Master's Thesis





Energy Technology
Aalborg University
<http://www.aau.dk>

AALBORG UNIVERSITY

STUDENT REPORT

Title:

Numerical investigation of the wavy channel geometry and its effect on heat transfer performance in natural convection flow

Theme:

Master Report

Project Period:

Spring 2020

Project Group:

TEPE4-1000

Participant(s):

Bjørn Christian Dueholm
Andreas Stengaard Thorstensen

Supervisor(s):

Jakob Hærvig
Henrik Sørensen

Page Numbers: 82

Date of Completion:

29th of May 2020

Abstract:

In this study natural convection in wavy channels is investigated. The channels are formed using sine waves with one wall phase shifted by $\phi = \pi$. The channels are defined by the dimensionless amplitude h/W and the dimensionless wavelength L/W . The simulations are conducted using DNS and the channels are simulated at a channel Rayleigh number $Ra_W' = 20000$. A parametric study is performed varying h/W from 0.02 to 0.08 and L/W from $5/3$ to $5/7$. The results show that increasing h/W and decreasing L/W generally lowers the surface averaged Nusselt number. Furthermore, the local Nusselt number follows the geometry rising as the channel converges and vice versa. All channels with $h/W = 0.02$ have a slightly higher \overline{Nu}_W with the largest increase being 0.35 %. Finally, it is found that channels of high amplitude/low wavelength increase heat transfer compared to a vertical channel.

The content of this report is freely available, but publication (with reference) may only be pursued due to agreement with the author.

By accepting the request from the fellow student who uploads the study groups project report in Digital Exam System, you confirm that all group members have participated in the project work, and thereby all members are collectively liable for the contents of the report. Furthermore, all group members confirm that the report does not include plagiarism.

Executive summary

Electronics cooling is one of the most widely spread engineering applications used in fields such as telecommunication and consumer electronics. In general low wattage electronics equipment is cooled by natural convective vertical channel heat sinks in air, where the effectiveness of the heat sink is limited by the thermal resistance due to the natural convective flow. Consequently, a lot of work has been devoted to the identification of geometries capable of increasing the convective heat transfer. One way of increasing the heat transfer is by introducing geometries that alter the flow increasing mixing, or by increasing the surface area based on the projected length of the channel. The present work seeks to investigate the heat transfer performance of the wavy channel geometry compared to the conventional vertical channel heat sink. An example of the velocity alterations between a vertical channel and a wavy channel is shown in Figure 1.

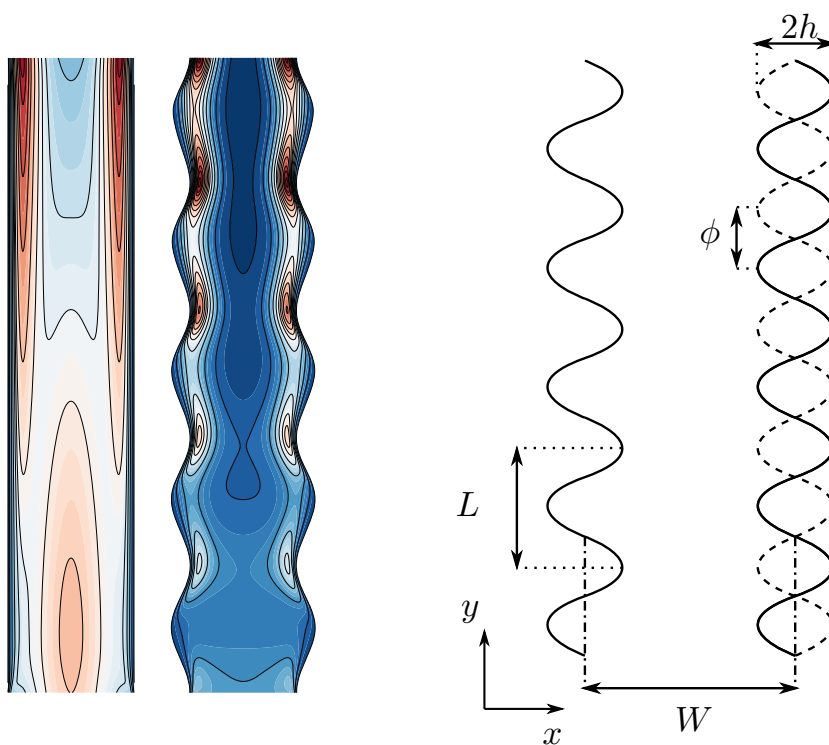


Figure 1: Example of the flow alterations created due to the implementation of a wavy channel geometry. The acceleration and deceleration of the flow together with the area increase of the wavy channel is the main contributor to the heat transfer enhancement.

Figure 2: Wavy parametric domain seeking to enhance natural convective flow.

The wavy shape of the channel is easily altered, changing the flow conditions within

the channel significantly, which means that the heat transfer performance of the channels depends greatly on the geometrical setup of the domain. Consequently, a numerical parametric study is performed using Direct Numerical Simulations (DNS), by changing the dimensionless amplitude (h/W) and dimensionless wavelength (L/W). The domain of the study is reduced to include one heat sink channel as shown in Figure 2. The DNS setup is validated by comparison with vertical channel studies in the literature before performing the parametric study of the wavy geometry. Here, the local Nusselt number Nu_W of the channels obtained with the present DNS setup and the simulations of Desrayaud and Fichera [2002] is presented in Figure 3.

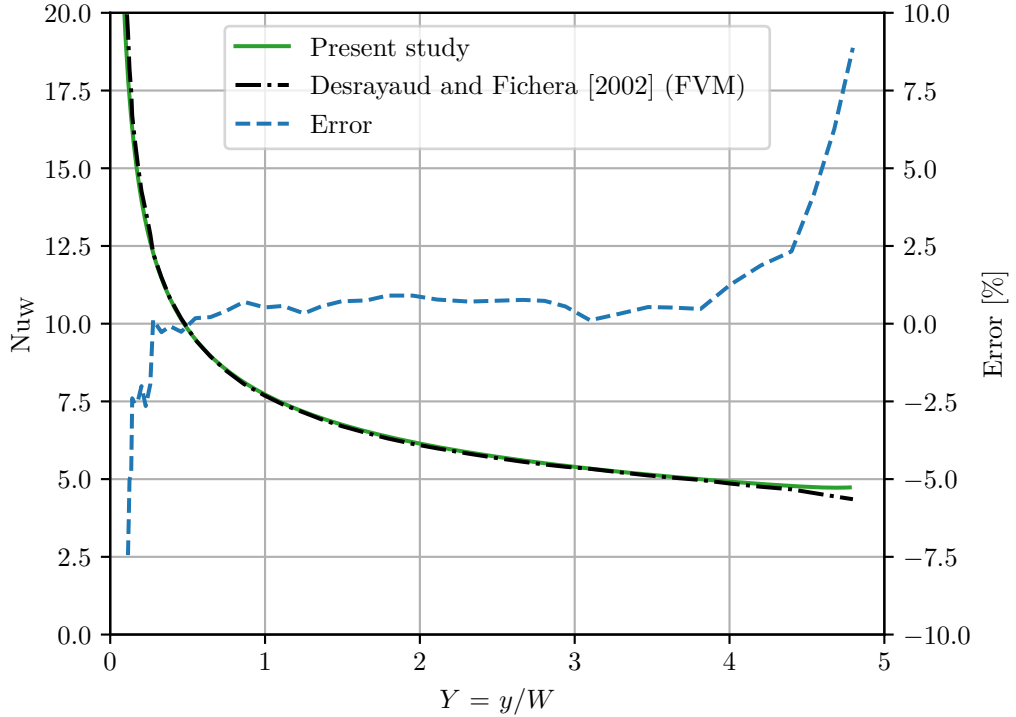


Figure 3: Comparison of the local Nusselt number, Nu_W , as a function of the dimensionless y -coordinate $Y = y/W$. All studies are conducted using the same aspect ratio of $a = 5$, and $Ra'_W = 2 \cdot 10^4$. The present study is compared to the numerical FVM study presented by Desrayaud and Fichera [2002]. As the data is quite comparable, an additional curve is included in the figure showcasing the error between the two studies.

The obtained data show excellent agreement, and the numerical setup is therefore used in the parametric study of the wavy geometry. The study of the wavy geometries show that a general decrease in the surface averaged Nusselt number is obtained at all combinations of h/W and L/W , except when $h/W = 0.02$ where a slight increase is observed. As mentioned earlier, the overall heat transfer of the channel can be increased by a combination of increasing the heat transfer coefficient and area. To

evaluate the heat transfer performance of the wavy geometry relative to the reference vertical channel (VC), a performance parameter denoted Q_{ratio} is introduced. The performance parameter is given in Equation 1.

$$Q_{\text{ratio}} = \frac{\overline{\text{Nu}}_W}{\overline{\text{Nu}}_{W,\text{VC}}} \cdot \frac{A}{A_{\text{VC}}} \quad (1)$$

Here $\overline{\text{Nu}}_W$ represents the surface averaged Nusselt number, while A represent the total area of the wavy geometry, and A_{VC} is the area of the vertical channel. The performance parameter for the different simulations are summarized in the contour plot shown in Figure 4.

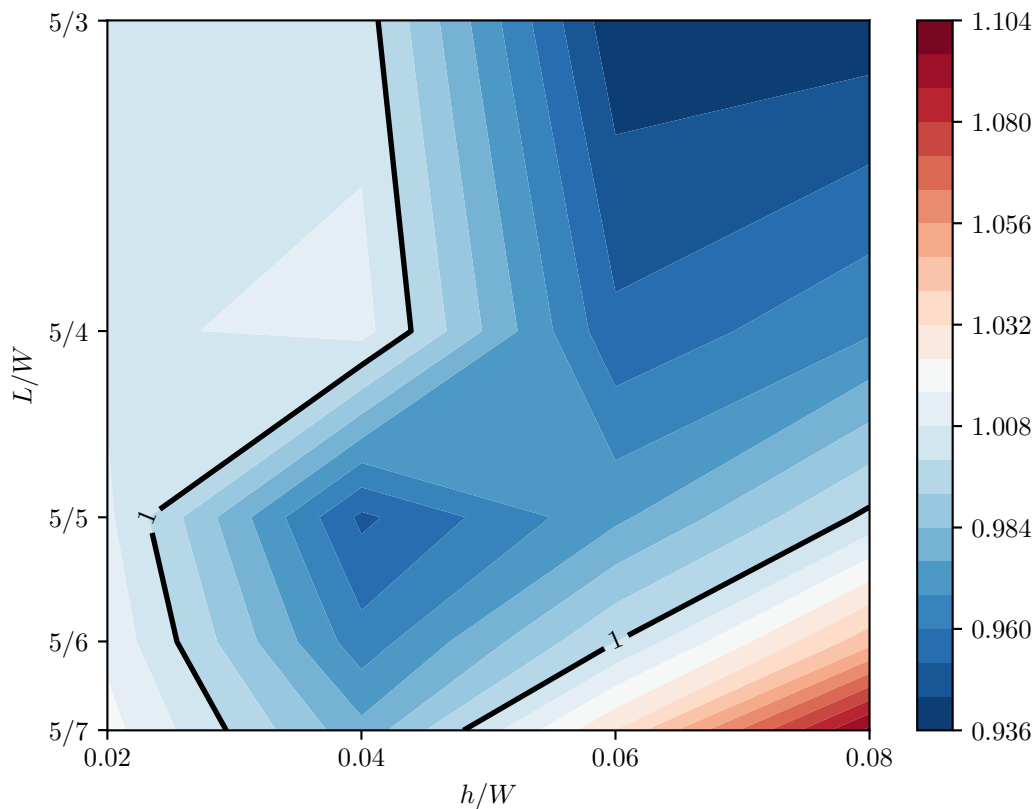


Figure 4: Contour plot of Q_{ratio} as a function of L/W and h/W . Here the different values of L/W and h/W are utilized to obtain values of A_{ratio} and $\text{Nu}_{W,\text{ratio}}$.

The investigations show that a significant increase in heat transfer is obtained at large amplitudes combined with a small wavelength. This behaviour is attributed to the large increase in surface area compared to the vertical channel.

Preface

This Master's Thesis is written by group TEPE4-1000, comprised of two energy engineering students from Aalborg University in the period from the 3rd of February 2020 to the 29th of May 2020. This report concludes the 4th semester of the M.Sc in Thermal Energy and Process Engineering at the department of Energy Technology. The project has been carried out with the guidance of Jakob Hærvig, Assistant Professor, Aalborg University and Henrik Sørensen, Associate Professor, Aalborg University.

Reading instructions

The report makes use of references according to the Harvard method. The references will occur in the text in the following manner: [Surname/publisher, year (possible page number)], where the end of the report is a comprehensive list of literature.

Reference numbers are made as hyperlinks in the digital copy. Figures and tables are listed as the chapter number, followed by the figure/table/equation number, as an example Figure 7.2 is the second figure in Chapter 7. Figure and table explanatory text can be found below the figure and above tables. Furthermore, section references are made using the section numbering. The unit system used in the report is the SI system with a dot as decimal separator. All figures without references are created by the authors.

During this project a CFD model was developed, which can be found in the digital appendix and requires a working installation of OpenFOAM 6 to view and run.

Nomenclature

Symbols

α	Thermal diffusivity	$\text{m}^2 \text{s}^{-1}$
β	Thermal expansion coefficient	K^{-1}
g	Gravitational acceleration vector	m s^{-2}
U	Velocity vector	m s^{-1}
U'	Dimensionless velocity vector	-
γ	Skewness	-
GCI	Grid convergence index	-
Gr	Grashof number	-
Nu	Nusselt number	-
Nu_W	Local Nusselt number based on W	-
Nu_y	Local Nusselt number based on local y-coordinate	-
Pr	Prandtl number	-
Ra'	Channel Rayleigh number = $(g\beta\Delta TW^3/\nu^2) \cdot W/H$	-
Ra	Rayleigh number = $g\beta\Delta TW^3/\nu^2$	-
ν	Kinematic viscosity	$\text{m}^2 \text{s}^{-1}$
ω	Placeholder variable used to indicate an obtained value in GCI	-
$\overline{\text{Nu}}_W$	Surface averaged Nusselt number based on W	-
$\overline{\text{Nu}}_y$	Surface averaged Nusselt number based on local y-coordinate	-
ϕ	Sine wave phase shift	rads
ψ	Placeholder variable used in the evaluation of GCI	-
ρ	Density	kg m^{-3}
Θ	Inclination angle	$^\circ$
θ	Dimensionless temperature	-
ζ	Grid cell size	m

A	Area	m^2
a	Aspect ratio = H/W	-
e	Relative errors between different grid refinements	-
F_s	Safety factor used in the evaluation of GCI	-
H	Channel length	m
h	Sine wave amplitude	m
h_c	Convective heat transfer coefficient	$\text{W m}^{-2} \text{K}^{-1}$
k	Thermal conductivity coefficient	$\text{W m}^{-1} \text{K}^{-1}$
L	Sine wave wavelength	m
L_c	Characteristic length	m
p_a	Apparent order of accuracy	-
p_{rgh}	Dynamic pressure	$\text{kg s}^{-2} \text{m}^{-1}$
q	Surface heat flux	W m^{-2}
r	Grid refinement ratio	-
T	Temperature	K
u	Velocity in the x-direction	m s^{-1}
v	Velocity in the y-direction	m s^{-1}
W	Channel width	m
X	Dimensionless x-coordinate = x/W	-
x	x-coordinate	m
Y	Dimensionless y-coordinate = y/W	-
y	y-coordinate	m

Subscripts

∞	surroundings
1	Fine grid
2	Medium grid
3	Coarse grid

cor	Correlation
in	At inlet
i	i'th entry
out	At outlet
ratio	Ratio between the present case and the vertical channel
VC	Vertical channel
W	Value based on the channel spacing W
w	At the wall
y	Local value based on y-coordinate

Abbreviations

CFD	Computational Fluid Dynamics
DNS	Direct Numerical Simulation
FVM	Finite Volume Method
GCI	Grid convergence index
SIMPLE	Semi- Implicit Method for Pressure-Linked Equations
UWT	Uniform wall temperature
VC	Vertical channel

Contents

Preface	ix
Nomenclature	xi
1 Potential of natural convection	1
1.1 Existing work on natural convection channel flow	2
2 Scope of project	7
2.1 Problem solving strategy	8
2.2 Determination of a viable Rayleigh number	10
3 Numerical approach	13
3.1 Modelling approach and governing equations	13
3.2 Meshing considerations	14
3.3 Dimensionless solution parameters	17
3.4 Numerical validation	19
3.4.1 Validation of numerical approach	19
3.4.2 Validation of natural convective channel flow	24
4 Numerical parametric study	29
4.1 Parametric geometry	29
4.2 Flow and temperature considerations	30
4.3 Evaluation of the wavy channel heat transfer performance	34
4.3.1 Evaluation of the heat transfer coefficient	34
4.3.2 Area increase due to wavy channel walls	37
5 Summary and discussion of results	41
5.1 Construction of a wavy channel array	42
6 Conclusions	45
A Literature review	47
B GCI calculations	53
C Python script used for mesh generation	55
Bibliography	63

1 | Potential of natural convection

At present time, there is a large emphasize on the world-wide electrification, which entails an increase in the amount of electrical components on a global scale. An increase in the amount of electrical equipment world wide naturally requires an equal amount of additional components capable of cooling the equipment. Convection heat transfer is commonly used for such applications as it is possible to cover a wide range of temperature ranges and heat fluxes as shown in Figure 1.1.

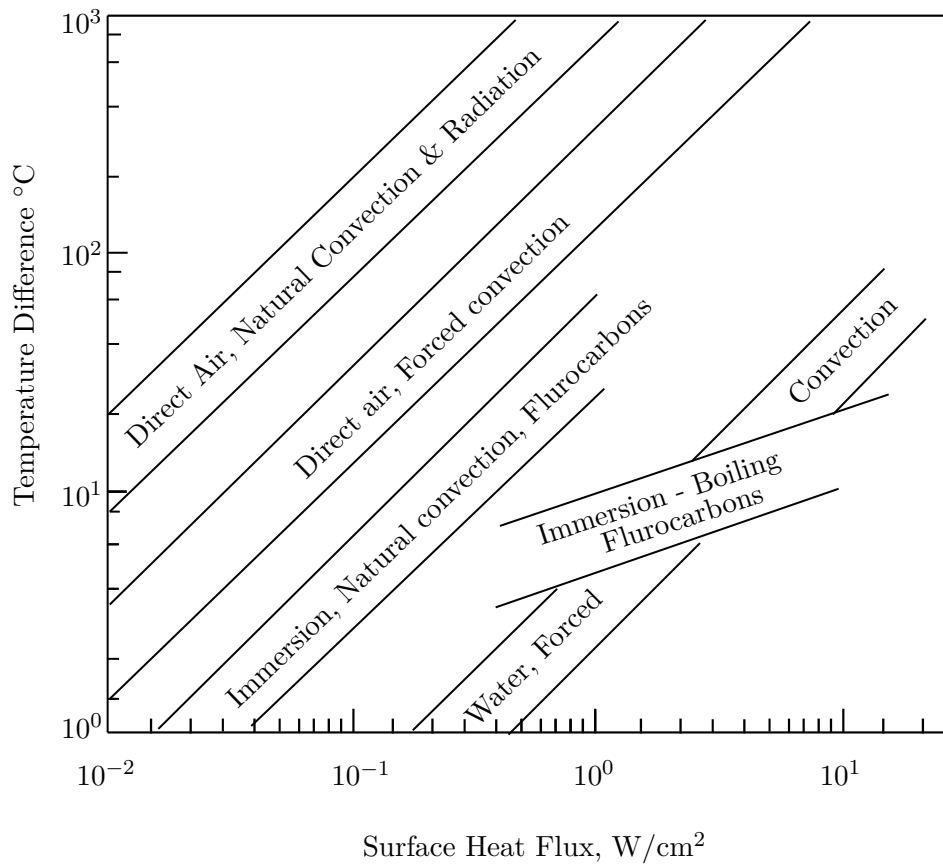


Figure 1.1: Temperature differences as a function of heat flux for different heat transfer techniques. [Kraus and Bar-Cohen, 1983]

As seen from Figure 1.1, numerous different convective heat transfer mechanisms are applicable in the cooling of electronics. Some are easier to implement than others, with natural convection in air being the simplest to implement. Natural convection excels in the area of cooling low wattage equipment, while forced convection with different fluids excel at cooling medium- to high-wattage equipment. To fur-

ther increase the heat transfer at lower temperature differences it is also possible to implement immersion phase change cooling, which is rather difficult in smaller components. The difference in heat transfer capabilities of natural- and forced convection can be found in the velocity of the moving fluid, as larger velocities in general result in larger heat transfer coefficients. In this way forced convection is in general superior to natural convection heat transfer, which is also seen from Figure 1.1 [Cengel, 2003]. Consequently, it is important to know the specific heat requirements of a component before deciding on a given convective heat transfer method and fluid. Generally it is more common to utilize forced convection for cooling of computer CPUs, as the heat dissipation of these components reach values in the order of 1-10 W/cm². A heat dissipation of 1-10 W/cm² requires a large temperature difference for natural convection to work, as shown in Figure 1.1, which inevitably makes natural convection not ideal for such applications. Such high values are difficult to reach using relatively small natural convective heat sinks, as the heat dissipation of such heat sinks increases with area. In this way the higher convective heat transfer coefficient of forced convection allows for a smaller heat sink that fits into a computer case easily. Some of the added cons of forced convection is the addition of moving parts in the form of a fan or pump, which is not a reliability issue encountered in natural convective heat sinks. On the other hand, natural convective heat sinks tend to require a larger temperature difference in order to meet the same heat dissipation, which reduces the reliability of the component due to higher temperatures. [Cengel, 2003]

The general trend for electronic components is, that they are becoming smaller due to the increasing demand for miniaturization of electronic equipment. As the size of the component, reduces the heat dissipation per area increases assuming that the equipment is required to abide by the same requirements. This behaviour continually increases the demand for cooling of electronic equipment. Since forced convection and immersion cooling is not applicable in every situation, natural convection will see a lot of use due to its simple and very reliable nature. Consequently, it becomes apparent that an optimization of the possible heat transfer due to natural convection would benefit the heat sink style mechanisms substantially.

As it is not within the scope of this study to investigate the improvement of all convective heat transfer mechanisms in cooling of electronics equipment, this study will focus on the natural convective mechanism. A review of the existing work within natural convective flow is given in Section 1.1.

1.1 Existing work on natural convection channel flow

In Appendix A the literature study conducted in this project is presented, where field of investigation, methods used and references of each of the chosen articles is shown. Based on this review, Figure 1.2 shows some of the more common geometries

studied regarding natural convective channel flow in the literature. The channel flow is especially interesting as it resembles most of the widely used heat sinks and arrays of PCBs.

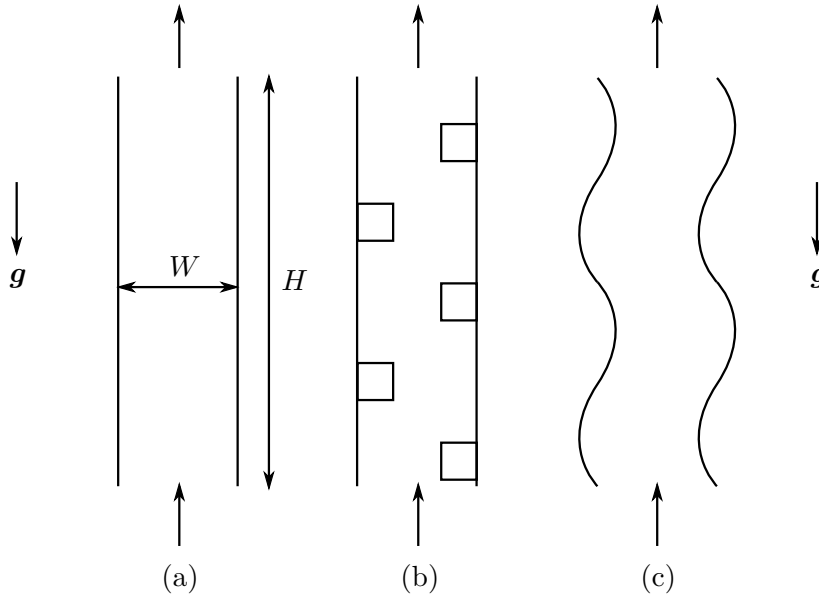


Figure 1.2: Most common geometries investigated in the literature. Here (a) is the common vertical plate channel, (b) introduced additional ribs to the vertical channel and (c) changes the channel completely by introducing wavy surfaces.

It is evident from the literature study that the largest amount of effort has been devoted to the geometry (a) shown in Figure 1.2. Figure 1.2a resembles the most common heatsink- and cavity geometry which explains the large effort. Consequently, both numerical and experimental studies have been conducted, where especially the length of the channel (H) and the spacing of the plates (W) have been of interest. Studies such as Roy et al. [2019] and Talukdar et al. [2019] also include the variation of the channel inclination angle to show the flow behaviour and temperature distribution in an angled channel. Roy et al. [2019] investigates the change in average Nusselt number as a function of inclination angle with a variable property fluid at different Grashof numbers, namely $Gr = 1.82 \cdot 10^5$ and $4.42 \cdot 10^5$. Here three different inclination angles are studied, namely $\Theta = 30^\circ, 45^\circ, 60^\circ$, and it is found that the 60° inclination case yields the highest average Nusselt number at all fluid property variations. This suggests that the heat transfer reaches a maximum as the inclination angle gets closer to 90° (vertical position). This is also expected as the velocity along the walls in the channel will drop as consequence of the channel being angled. Consequently, the closer the channel is to being completely horizontal, the lower the heat transfer is expected to be. Additionally, Talukdar et al. [2019] investigates the flow and heat transfer of channels at different inclinations angles and channel Rayleigh numbers. Here the inclination angle range include $10\text{-}90^\circ$ compared to the horizontal axis, and

the channel Rayleigh number range of $Ra'_W = (g\beta\Delta TW^4/\nu^2H) \cdot Pr = 62-16000$. The study is conducted using a high temperature difference of 110 °C compared to the ambient temperature, and is therefore compressible. It is found that the average Nusselt number based on the channel width increase with the channel Rayleigh number ($Ra'_W = Ra_W \cdot W/H$), and as the inclination angle increases towards 90°, which is in good agreement with Roy et al. [2019].

As the vertical parallel plate channel is the geometry frequently used in the industry, numerous studies have been carried out in the search of better geometrical configurations. Here Figure 1.2b and 1.2c show some of the more common alternatives investigated in the literature.

Figure 1.2b represents a vertical channel where additional periodic ribs have been introduced. Numerous studies are present in the literature regarding increase in performance due to ribs. For this short review, two studies investigating the effect of ribs on heat transfer performance have been chosen, namely Abidi-Saad et al. [2016] and Tanda [1997]. Abidi-Saad et al. [2016] investigates the influence of a symmetrically positioned pair of ribs on the flow structures and convective heat transfer coefficient in a channel at $Ra'_W = 3.65 \cdot 10^6 - 4.4 \cdot 10^6$ based on a constant heat flux. The ribs are moved between three positions in the channel (top, middle and bottom), and the flow structures and heat transfer are obtained experimentally using PIV imaging. It is found from the study that large instabilities are formed due to the ribs at all values of Ra'_W , and that the heat transfer performance depends strongly on the position of the ribs together with Ra'_W . The heat transfer coefficient results are compared to the vertical plate channel heat transfer coefficient for all cases, and it is found that positioning the ribs in the top results in a larger average heat transfer coefficient for low to moderate value of Ra'_W , while the middle position is best suited for high values of Ra'_W . Tanda [1997] has a similar approach, but utilize Schlieren imaging to obtain the experimental results for ribbed channels at $Ra'_W = 2 \cdot 10^2 - 5 \cdot 10^5$. The results are again compared to the channel with vertical walls, where results for the ribbed channels are obtained for different modified channel aspect ratios ($W/H = 0.4, 0.1$ and 0.05 , where W is the channel spacing and H is the channel length). From the results it is clear that the heat transfer performance of the smooth plate channel is superior to the ribbed channel case, because the local increase in heat transfer from introducing the ribs, is less than the local decrease in heat transfer from the low velocity zones the ribs create. It is therefore concluded that the introduction of ribs does not benefit heat transfer, in the range of parameters investigated.

The geometry shown in Figure 1.2c represents a special case of a vertical channel with walls following a sinusoidal nature. Few studies look into this geometry in natural convection, but the geometry is widely investigated in forced convection due to its resemblance of corrugated plates used in heat exchangers etcetera. A single study has been found on the wavy channel flow due to natural convection, namely Altun

and Ziylan [2019]. Altun and Ziylan [2019] is an experimental study comparing the heat transfer performance of heat sinks with and without fins. Two types of fins are investigated, namely vertical plate- and wavy sinusoidal fins in a Rayleigh Number range from $Ra_W = 2 \cdot 10^5$ to $3 \cdot 10^6$. The wavy finned geometries are changed according to the amplitude of the sinusoidal curve ($h = H/30, H/15, H/10$) where h is the amplitude and H is the channel length. The reported results show that the wavy fin heat sink with $h = H/30$, and $h = H/15$, performs better than the rectangular fin heat sink at all Ra_W value cases, while the rectangular fin case outperforms the wavy fin with $h = H/10$ at $Ra = 2.4 \cdot 10^6$. Furthermore, it is found that the rectangular fin case outperforms the un-finned plate in the complete range of Ra_W . This shows a possible improvement of the heat transfer performance of a heat sink due to the introduction of wavy channel walls. To extend upon the relatively scarce literature regarding natural convective flow in wavy channels, a single wall investigation conducted by Bhavnani and Bergles [1991] has been included. Bhavnani and Bergles [1991] investigates the heat transfer performance of a wavy surface compared to the vertical plate alternative using the experimental Mach-Zehnder interferometer (MZI) procedure. The study is conducted at relatively high values of $Ra_y = (g\beta\Delta T y^3/\nu^2) \cdot Pr$, in order to find a transition to unsteady flow. The study presents its results in two ways, one based on projected area the other based on actual length of the surface under investigation. This procedure is introduced to take into account that the wavy surface in general has an increased total length based on projected area than the vertical plate surface. Using this method, the study conducted by Bhavnani and Bergles [1991] conclude that the wavy surface transfers more heat compared to the flat vertical surface based on projected area, while the vertical plate transfers more heat based on actual length of the plate.

2 | Scope of project

From the literature study shown in Section 1.1 it is evident that a large effort has been devoted to natural convective flow. It is furthermore shown that the effort is divided mainly into the vertical plate channel, but also into various geometries seeking to enhance the heat transfer effects of the channel flow. The most common geometry investigated to enhance heat transfer is the addition of ribs. The ribs are either introduced in pairs at the same vertical channel location, or shifted in order to affect the flow in different ways. The ribbed channel results are contradictory as Abidi-Saad et al. [2016] reports an increase in heat transfer while Tanda [1997] reports a decrease in heat transfer. In this way it appears that the heat transfer enhancement due to ribs depend strongly on both the geometry and Rayleigh number range investigated. The final, and less common geometry investigated in this study is the introduction of wavy channel walls. Here the results reported by Altun and Ziylan [2019] and Bhavnani and Bergles [1991] indicate an increase in heat transfer due to the introduction of the wavy channel walls compared to the vertical plate walls. It is however reported in Bhavnani and Bergles [1991], that the wavy plate only increases heat transfer based on projected area, and not based on actual length of the plate compared to the vertical plate. Therefore, this study aims to investigate the wavy channel arrangement. The wavy channels have the potential to increase heat transfer, not only by adding more area, but also by disturbing the flow. Based on the wavy channel geometry, it is desired to perform a parametric study to investigate how the sine wave amplitude and wavelength affect the flow, and further how these flow alterations affect the heat transfer performance of the channel. The definitions of amplitude, phase shift, and wavelength of the parametric geometry are shown in Figure 2.1. The phase shift of the sine wave is expected to have an effect on the flow, but it has been neglected in the present study to decrease its size. Consequently, the phase shift of the right sine wave wall is constant at $\phi = \pi$.

Computational Fluid Dynamics (CFD) is used to model the flow and heat transfer of the geometry as it provides the flexibility needed to conduct the parametric study. It is desired to compare the CFD model against other similar studies in order to ensure the validity of the model before moving into the wavy channel cases. This leads to the problem statement of this study:

How does the amplitude and wavelength affect the developing natural convective flow and thereby the heat transfer in a channel formed by two identical sine waves?

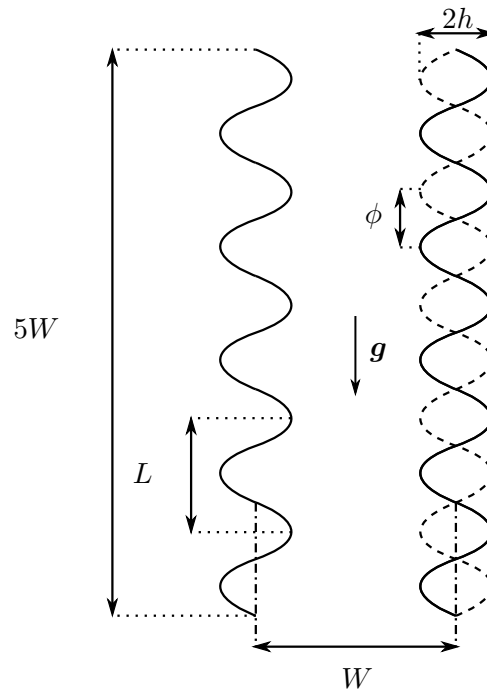


Figure 2.1: Here ϕ is the phase shift of the sine wave used to form the channel walls. The phase shift is applied to the right wall, with a phase shift of 0 corresponding to identical channel walls. Depicted in the figure is a phase shift of $\phi = \pi$, as shown by the dotted line (- - -). Furthermore, h represents the amplitude of the sine wave, W represents the channel width taken as the distance between the center lines of the sine waves as shown by the dotted line (-·-) and L represents the wavelength of the sine wave. The aspect ratio, denoted $a = (H/W)$, of the channel is held constant at 5.

2.1 Problem solving strategy

Before moving into the parametric study, several subtasks have to be completed. The subtasks mainly focus on the numerical approach used to form the final setup, before it is utilized in the parametric study. The numerical approach seeks to analyze the flow in the channel by the use of CFD simulations. The simulations are all conducted in the open source CFD software OpenFOAM. To develop a CFD setup capable of analyzing the present channel flow, the following tasks are addressed.

- Determination of applicable CFD modelling approach for the present study including solution model and spatial discretization.
- Construction of a script capable of generating suitable computational grid files applicable by the blockMesh structure in OpenFOAM
- Determination of suitable dimensionless solution parameters to evaluate heat transfer and flow distribution

- Validation of the mathematical approach including boundary conditions and grid convergence.

The first task is to identify which numerical approach of the three most common, namely Direct Numerical Simulation, Large Eddy Simulation and Reynolds-Averaged Navier-Stokes is best suited for the case presented in this study. Furthermore, it is included in this task to choose appropriate discretization schemes to resolve the spatial calculations. The second task is the creation of an appropriate numerical grid suitable for the blockMesh environment utilized by OpenFOAM. Here Python is used to develop the parametric geometry and associated grid files utilized by blockMesh to construct both validation cases and the parametric study domains. The third task seeks to investigate appropriate solution parameters used to evaluate heat transfer and flow distribution. Here it is desired to compare geometrical alternatives by the use of dimensionless parameters due to their comparability with the literature. The fourth task includes both validation of the numerical approach, including boundary conditions, and the grid convergence study. The validation of the numerical approach is crucial as it investigates the accuracy of the applied model and discretization schemes chosen in the first task, together with the boundary conditions used to resemble unconfined flow. To further increase the validity of the solution, it is investigated at which grid refinement the solution approaches an asymptotic value independent of the grid. The grid convergence study is performed by increasing the amount of cells used to refine the flow until an asymptotic value of the solution parameter is obtained. The independent grid is then used as the base grid for the parametric study. The overall structure of the report leading up to the parametric study is shown in Figure 2.2.

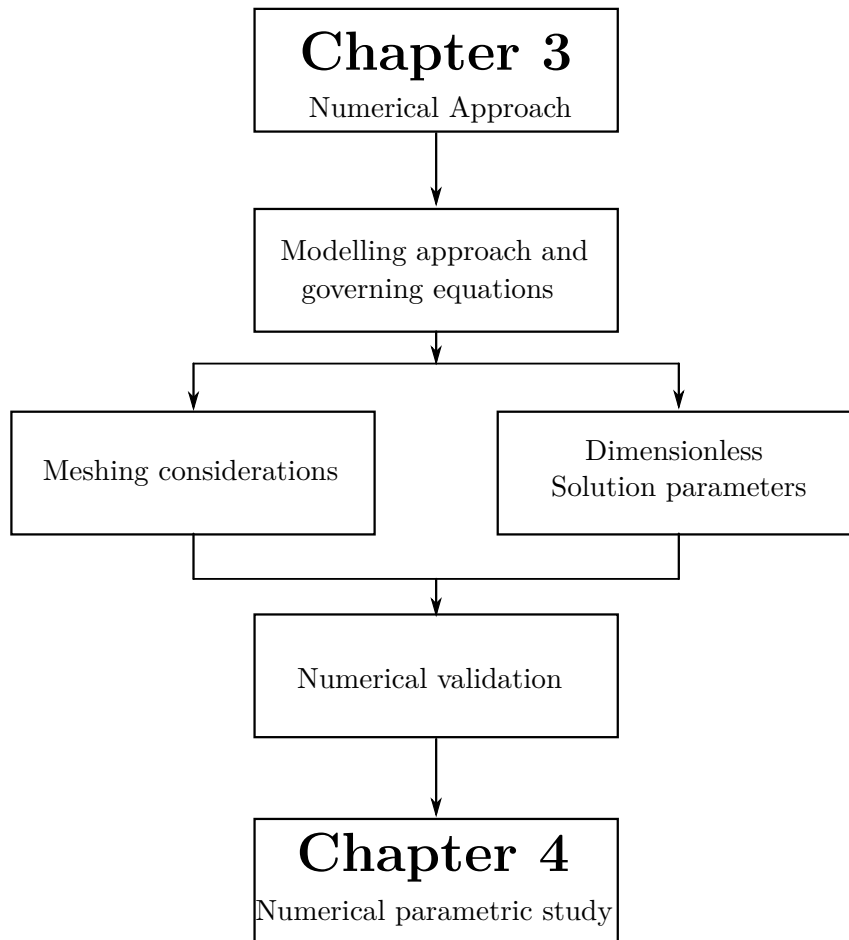


Figure 2.2: Visual overview of the report structure.

2.2 Determination of a viable Rayleigh number

In order to conduct the parametric study, it is necessary to estimate a Rayleigh number. This section seeks to outline the creation of such a value based on the package temperatures of electronic equipment. Natural convective cooling of electronic equipment can be very different depending on the type of device in question. As an example there is a significant difference in the cooling of a PCB and an amplifier. The difference is mainly due to the heat dissipated from each device, where amplifiers in general dissipate significantly more heat than a PCB. Electrical devices are usually rated for certain package temperature ranges, where commercial (0 °C to 70 °C) and industrial (-40 °C to 85 °C) include the most common products used today [Mishra, 2004]. With these package temperature ranges in mind, and given a standard ambient air temperature range from 0 °C to 20 °C, a maximum temperature difference of 85 °C can be acquired. Using this temperature range, it is possible to

estimate a Rayleigh number range for electronic devices using Equation 2.1.

$$\text{Ra}_W = \text{Gr}_W \text{Pr} = \frac{g\beta\Delta T W^3}{\nu^2} \text{Pr} \quad (2.1)$$

Here g is the gravitational acceleration, β is the thermal expansion coefficient, ΔT is the temperature difference between the surface and surroundings, W is the channel width, ν is the kinematic viscosity, Pr is the Prandtl number, Ra_W is the Rayleigh number based on the channel width and Gr_W is the Grashof number based on the channel width. In order to visualize a possible range of Ra_W , a contour plot of Ra_W as a function of the temperature range and channel spacing is given in Figure 2.3.

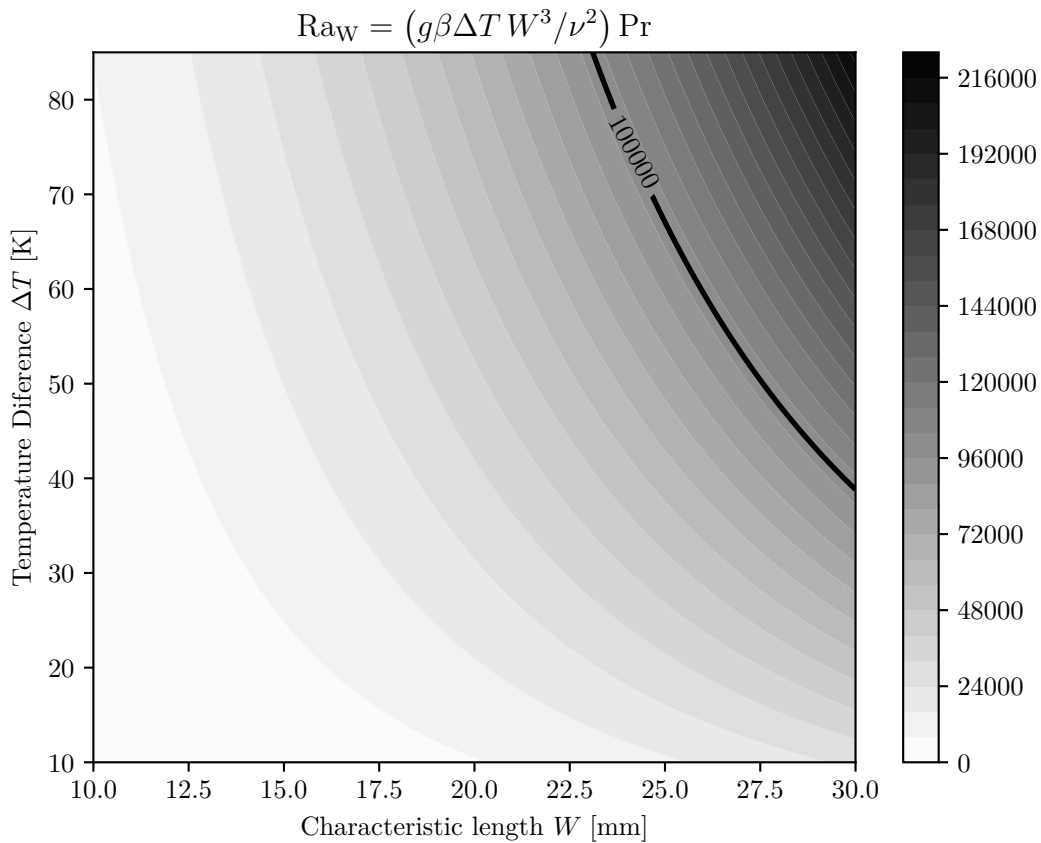


Figure 2.3: Contours of Ra_W as described by Equation 2.1, given the ranges of ΔT and W .

It is seen from Figure 2.3 that a large Ra_W range is obtained at smaller channel widths as Ra_W is a function of the channel width to the power of three. In this way Ra_W increases rapidly as the channel width increases. The given range of channel spacing used in this study from 10 mm to 30 mm represents relatively large

electronics equipment. As an example the channel spacing could be encountered in large amplifiers or telecommunication heat sinks. Here it is taken into account that a smaller channel width lowers the possible heat transfer coefficient due to natural convection significantly. Consequently, it becomes undesirable to lower the channel width to a certain extent as the heat transfer coefficient decreases with decreasing Ray_w . Using this range, a Rayleigh number range from around 1000 to around 220000 is obtained using the complete temperature difference range from 10 °C to 85 °C. This study then seeks to investigate a Rayleigh number of 100000, which is marked in the figure as the solid line.

3 | Numerical approach

This chapter seeks to outline the numerical procedures used to validate the model used for the final parametric study, as described in Chapter 4. First, the mathematical formulation in the form of the assumptions used to acquire the governing equations, simulations model, solver algorithm, discretization and mesh type used is outlined in Section 3.1. Next, the meshing procedures and solution parameters used to evaluate the different geometries are outlined in Section 3.2 and Section 3.3 respectively. Finally, two validation cases are outlined in Section 3.4. The two validation cases consider a vertical plate and a vertical channel respectively, both under natural convective flow with uniform wall temperature (UWT) at the wall/walls respectively. The validation cases are conducted to ensure that the numerical setup used for the parametric study of the plate shape is valid.

3.1 Modelling approach and governing equations

The validation cases considered in this chapter are all considering laminar and steady two dimensional air flow. As laminar flow is considered, this study has been conducted using the Direct Numerical Simulation (DNS) approach implemented in OpenFOAM. The mathematical model is described by the conservation of mass, momentum and energy equations, where an in-compressible model is utilized for the simulations. This is further coupled with the Boussinesq approximation, which assumes the density to be constant in all terms except the buoyancy term. These assumptions reduce the governing Navier-Stokes equations to the form shown in Equation 3.1-Equation 3.4 [Minocha et al., 2016].

$$\frac{\partial u}{\partial x} + \frac{\partial v}{\partial y} = 0 \quad (3.1)$$

$$u \frac{\partial u}{\partial x} + v \frac{\partial u}{\partial y} = -\frac{1}{\rho} \frac{\partial p}{\partial x} + \nu \left(\frac{\partial^2 u}{\partial x^2} + \frac{\partial^2 u}{\partial y^2} \right) \quad (3.2)$$

$$u \frac{\partial v}{\partial x} + v \frac{\partial v}{\partial y} = -\frac{1}{\rho} \frac{\partial p}{\partial y} + \nu \left(\frac{\partial^2 v}{\partial x^2} + \frac{\partial^2 v}{\partial y^2} \right) + \mathbf{g} (1 - \beta (T - T_\infty)) \quad (3.3)$$

$$u \frac{\partial T}{\partial x} + v \frac{\partial T}{\partial y} = \alpha \left(\frac{\partial^2 T}{\partial x^2} + \frac{\partial^2 T}{\partial y^2} \right) \quad (3.4)$$

Here the gravitational acceleration is parallel to the y-axis, hence it is only included in Equation 3.3. Furthermore, it is observed by comparing Equation 3.3 to the traditional Navier-Stokes equations, that the density in the buoyancy term has

been replaced by temperature. This replacement is governed by an approximation where a linear density temperature relation $\Delta\rho/\rho_0 = \beta(T_\infty - T)$ is used to obtain Equation 3.3.

An overview of the numerical approach including the solution method, discretization schemes, solver algorithm and mesh type is given in Table 3.1.

Table 3.1: Recap of the numerical approach used in the present study

Simulation method	DNS
Solver algorithm	SIMPLE
Discretization schemes	
Spatial	Central difference
Velocity	Gauss linear vanLeerV
Mesh type	Hexahedral

The governing equations are all implemented into OpenFOAM through the buoyant-Boussinesq type solvers, where the buoyantBoussinesqSimpleFoam solver is used to solve the steady, laminar flow in the validation cases described in Section 3.4.

3.2 Meshing considerations

This section seeks to outline some of the meshing considerations applied to form the grids of the validation cases and the parametric study. An overview of the three different domains is given through Figure 3.1(a), (b) and (c). Here the domains used for validating the numerical approach and natural convective channel flow are shown in Figure 3.1(a), (b) respectively, while Figure 3.1(c) shows an example of a wavy parametric domain.

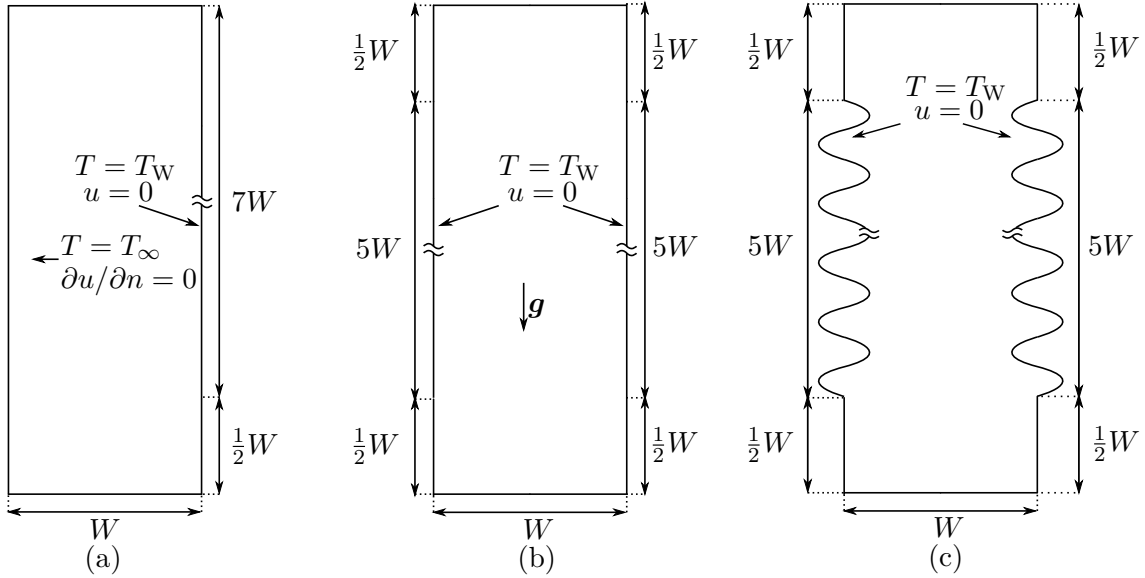


Figure 3.1: Geometries used in the two validation cases, namely (a) and (b) together with an example of a parametric geometry shown in (c). The two validation case grids are relatively simple as both domains contain perfect (zero skewness) hexahedral cells. The parametric geometry with the sine wave walls does however complicate the grid, increasing the skewness level of the associated grid.

The grids used in OpenFOAM are all created using blockMesh, with the blockMeshDict file generated in Python. The Python script generates the sine wave walls as splines between two endpoints, where one of the walls is shifted an amount equal to the channel width in the x-direction to form the channel. The splines and points used to define the channel is transferred to the blockMesh file by overwriting specific lines in a blockMeshDict template as shown in Appendix C. In order to increase stability of the numerical simulations, additional wall sections are introduced in the beginning of the numerical approach validation domain (Figure 3.1(a)), and in both the beginning and end of the channels used for the flow validation (Figure 3.1(b)) and parametric study (Figure 3.1(c)). This is done to reduce the effects of the inlet and outlet boundary conditions, and to reduce the likelihood of divergence if a recirculation zone is present at the end of, or in the beginning of the channel. The addition of the vertical section at the inlet and outlet does however introduce some difficulties in the transition of the grid, when a wavy geometry is implemented. Here it is crucial to attach the sine wave to the vertical section at the sine wave peak, as the angle between the vertical section and the tangent of the wavy section is zero at this sine wave location. An example of a generated grid for $\phi = \pi$ and $h/W = 0.08$ is shown in Figure 3.2. The grid created for the geometry with $h/W = 0.08$ and $\phi = \pi$ is chosen here as this is the grid where the largest change happens between the vertical and wavy sections.

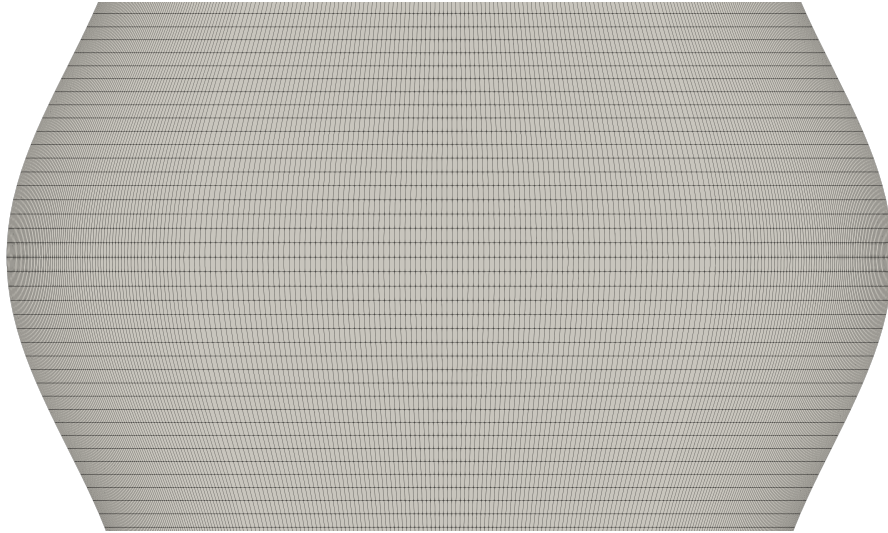


Figure 3.2: Grid of a section of the channel when the dimensionless sine wave amplitude h/W is 0.08 and $\phi = \pi$.

As noticed from Figure 3.2, an expansion ratio is applied towards the walls. This is done in order to reduce the amount of cells required to refine the domain, without compromising the wall adjacent cell size. The expansion ratio applied is equal to 4, which indicates that the near wall cell is four times smaller than the cell at the end of the meshing block. The domain is divided into three meshing blocks in the x-direction. The first and last sections include 60 % of the cells used to refine the x-direction of the domain over 40 % of the complete width of the domain. In this way 30 % of the cells are positioned in only 20 % of the x-direction domain. The remaining 40% of the cells are located in the middle of the domain consisting of the remaining 60 % of the domain. This is also indicated by the large section in the middle where there is no change in the cell size at specific values of the y-coordinate.

One of the common ways to evaluate the quality of the mesh is to report the skewness of the mesh. The skewness of the mesh is a measure of how parallel two vectors are relative to each other using the dot product [Stimpson et al., 2007]. In this way there are three different values of skewness for a hexahedral cell, namely one in each dimension (x,y,z), with the skewness defined as shown in Equation 3.5.

$$\gamma = \max(\text{skew}_i) \quad (3.5)$$

Here skew_i , where i denotes the x-, y- and z-directions, is the skewness obtained for the hexahedral cell relative to each coordinate axes. The skewness of the cell γ , is then taken as the maximum value of each contribution and reported in the range between 0 and 1. An acceptable value of skewness for a hexahedral grid is below 0.5 [Stimpson et al., 2007]. A histogram of cell skewness obtained from the geometry with $h/W = 0.08$ and $\phi = \pi$ is shown in Figure 3.3.

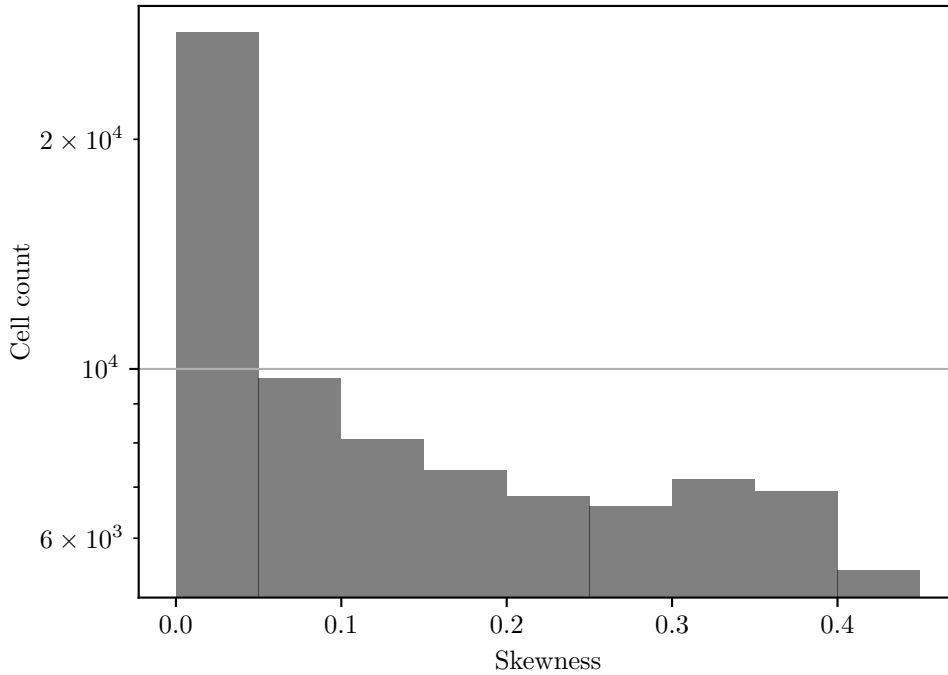


Figure 3.3: Histogram of the cell skewness when the dimensionless sine wave amplitude h/W is 0.08 and $\phi = \pi$

As seen from Figure 3.3, the maximum skewness of the grid amounts to approximately 0.45 which is below 0.5. As the geometry is periodic throughout, it is furthermore observed that the cell count in some skewness ranges is relatively large with peaks in the $[0; 0.05]$ and $]0.05; 0.1]$. Here the cell count reaches approximately 10^4 or above. This concludes the meshing procedures used in this study, the next section will present the solution parameters used to evaluate the heat transfer coefficient and fluid motion in both validation cases and the parametric geometries.

3.3 Dimensionless solution parameters

In order to evaluate the performance of the validation geometries and compare the obtained results with the literature, multiple solution parameters are included in the validation study. As most data in the literature focus on the heat transfer performance, the Nusselt number is commonly reported. Consequently, the Nusselt number has been adopted as the global solution parameter for the validation cases and parametric study. As the geometries studied in this chapter include both a vertical plate and a vertical plate channel, two separate definitions of the Nusselt number is required. The main difference between the definitions is the characteristic

length used for the geometry. The most common geometrical entity used for vertical plates is the local channel height, denoted y , while the channel width, denoted W is the more common entity used for channels. The general definition of the Nusselt number used in this study is shown in Equation 3.6.

$$\text{Nu} = \frac{hL_c}{k} = \frac{\partial T}{\partial n} \frac{L_c}{T_w - T_\infty} \quad (3.6)$$

Here T_w is the wall temperature, T_∞ is the temperature of the surroundings, L_c is the characteristic length of the geometry and $\partial T/\partial n$ is the temperature gradient normal to the wall. Furthermore, it should be noted that the temperature gradient $\partial T/\partial n$ is found as a local value at every cell along the wall. Using the definition of the Nusselt number presented in Equation 3.6, it is possible to establish the definitions of the local Nusselt numbers for the vertical plate and channel as shown in Equation 3.7 and 3.8 respectively.

$$\text{Nu}_y = \frac{hy}{k} = \frac{\partial T}{\partial n} \frac{y}{T_w - T_\infty} \quad (3.7)$$

$$\text{Nu}_W = \frac{hW}{k} = \frac{\partial T}{\partial n} \frac{W}{T_w - T_\infty} \quad (3.8)$$

With these definitions of the local Nusselt number for the vertical plate and channel respectively, it is possible to extend upon the definitions to obtain a surface averaged Nusselt number as shown in Equation 3.9 and 3.10 for the vertical plate and channel respectively.

$$\overline{\text{Nu}}_y = \frac{\int_A \text{Nu}_y dA}{\int_A dA} \quad (3.9)$$

$$\overline{\text{Nu}}_W = \frac{\int_A \text{Nu}_W dA}{\int_A dA} \quad (3.10)$$

Here the surface averaged Nusselt numbers reported in Equation 3.9-3.10 are used as benchmark values for the evaluation of grid convergence of each validation case.

Since the Nusselt number primarily focus on the evaluation of the heat transfer coefficient, two additional parameters are introduced, namely the dimensionless velocity vector and the dimensionless temperature in order to evaluate the flow conditions in the channels. The definition of the dimensionless velocity \mathbf{U}' , is given in Equation 3.11, while the dimensionless temperature θ , is given in Equation 3.12.

$$U' = \frac{U|U|}{|g|\beta(T_w - T_\infty)} \quad (3.11)$$

$$\theta = \frac{(T - T_\infty)}{(T_w - T_\infty)} \quad (3.12)$$

This concludes the choice of solution parameters used to evaluate the different domains. The next section seeks to outline the validation cases used to evaluate the applicability of the numerical approach, the associated boundary conditions and associated grids.

3.4 Numerical validation

This section seeks to investigate and subsequently validate the numerical approaches used to resemble truly unconfined flow for natural convective flows. The validation is divided into two cases, first a vertical plate is investigated in Section 3.4.1, followed by an investigation of natural convective flow in channels as described in Section 3.4.2. Both validations are compared to the literature to benchmark the validity of the numerical boundary conditions, schemes and grid employed in the simulations.

3.4.1 Validation of numerical approach

To ensure the choice of boundary conditions and schemes resemble truly unconfined flow, while also monitoring the discretization error, a validation case of a vertical plate has been constructed. To validate the numerical code based on the boundary conditions and associated grid, shown in Figure 3.4(a) & (b) respectively, two additional steps have been introduced. First, a grid convergence study is conducted to show the results dependence on grid size. Second, the local heat transfer performance of the vertical plate is verified against the analytical solution for a vertical plate at constant temperature.

Before proceeding to the grid convergence study, the domain together with the boundary conditions chosen to resemble unconfined natural convective flow is shown in Figure 3.4. The inlet and outlet boundary conditions are specified to follow the inletOutlet/outletInlet procedure in OpenFOAM. The inletOutlet/outletInlet procedure acts as a zero gradient boundary condition unless there is reverse flow. In case of reverse flow the temperature and velocity values are fixed to a specified value, in this case zero for velocity and T_∞ for temperature as indicated by the inlet value shown in Figure 3.4.

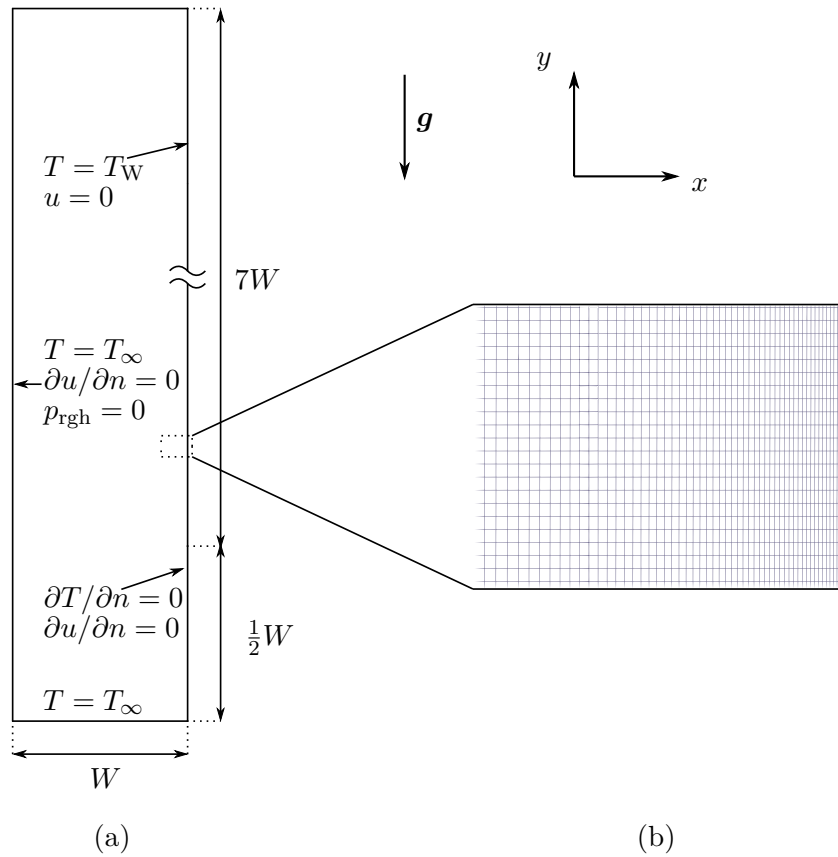


Figure 3.4: Here (a) describes the geometry and boundary conditions used for the vertical plate case, while (b) shows a cutout of the grid. From (a) it is shown that the heated wall section is elevated from the inlet by the length $1/2W$ in order to reduce the effect of the inlet conditions. The additional section has slip boundaries with regard to both temperature and velocity. The left wall section resembles the ambient surroundings at $T = T_\infty$ and $p_{\text{rgh}} = 0$. The heated wall is isothermal at $T = T_w$ with no slip on the wall. The grid cutout shown in (b) shows the grading used towards the wall in order to properly resolve the thermal boundary layer at the wall.

In general the boundary conditions are chosen to resemble unconfined flow, where the left wall boundary represent the surrounding fluid, hence the specified surrounding temperature of T_∞ , and specified pressure p_{rgh} . The right heated wall is kept at a constant temperature of T_w , with the no slip condition imposed for velocity. These boundary conditions and domain specifications are utilized for the grid convergence study, where three different grids have been created in order to obtain values of the surface averaged Nusselt number of the plate. Information about the different meshes is outlined in Table 3.2.

Table 3.2: Grid convergence study data for the three different grids, namely the coarse-, medium- and fine grid where each step increases the amount of cells by a factor of 4. The increase in cells is based on doubling the amount of cells in both the x-, and y-direction between each grid. Here \overline{Nu}_y is the surface averaged Nusselt number obtained by averaging the local Nusselt number (Nu_y) over the entire plate.

Grid	Wall expansion rate	Cell count	\overline{Nu}_y
Coarse (37 x 200 x 1)	4	7400	13.9314
Medium (75 x 400 x 1)	4	30000	13.9278
Fine (150 x 800 x 1)	4	120000	13.927

In Table 3.2, the average Nusselt number for the plate \overline{Nu}_y is calculated as shown in Equation 3.9. From Table 3.2, it is seen that the difference between the coarse and medium grid is greater than between the medium and the fine grid. This suggests that the solution approaches asymptotically towards a grid independent value as described in Celik et al. [2008]. A graphical representation of the obtained results is given in Figure 3.5.

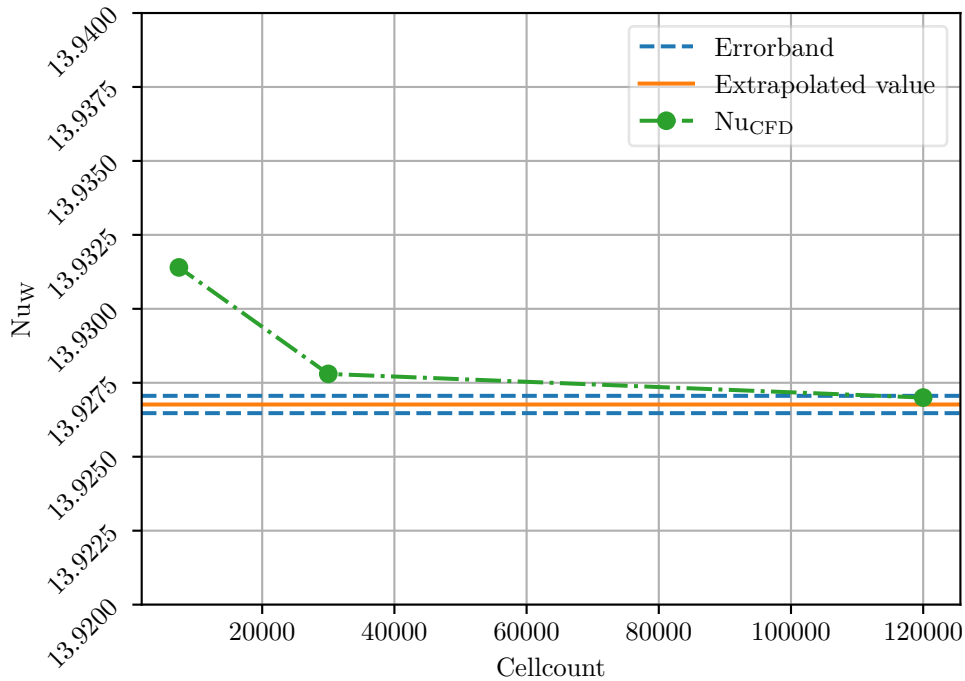


Figure 3.5: Development of the obtained results with grid refinement. Here the green curve ($-\cdot-$) shows the average Nusselt number, while the blue ($- - -$) and orange ($---$) lines are indicators of the criteria of convergence. Here the blue lines show the error-bands, while the orange line shows the extrapolated final value with a grid of infinite refinement.

Here the green curve ($-\cdot-$) shows the obtained \overline{Nu}_y values, while the blue ($- -$) and orange ($---$) curves respectively function as indicators for the error-bands and the extrapolated final value at an infinite grid refinement. The criterion for accepting a value as grid independent is for it to be within the error-bands and ensuring compliance with Equation 3.13, while still maintaining a relatively low value for the grid convergence index (GCI). Equation 3.13 is an indication of whether the solution approaches asymptotically towards a grid independent value.

$$\frac{GCI_{coarse-medium}}{r_{medium-fine}^p \cdot GCI_{medium-fine}} \approx 1 \quad (3.13)$$

The procedures used to obtain the necessary parameters shown in Equation 3.13 is given in Appendix B. Consequently, only the obtained data is given here through Table 3.3.

Table 3.3: Necessary data to show the convergence of the fine grid solution.

	coarse-medium	medium-fine
GCI	$9.3 \cdot 10^{-5}$	$2.1 \cdot 10^{-5}$
Equation 3.13	0.996	

As seen from Table 3.3, the GCI values together with the compliance with Equation 3.13 is satisfied for the final grid including 120 000 cells total. Consequently, this grid is utilized for the validation by comparing the results with the correlation described by Ostrach [1952] as shown in Equation 3.14.

$$Nu_{y,cor} = \left(\frac{Gr_y}{4} \right)^{1/4} g(Pr) \quad (3.14)$$

Here $Nu_{y,cor}$ is the local Nusselt number obtained from the correlation proposed by Ostrach [1952], and Gr_y is the local Grashof number given in Equation 3.15.

$$Gr_y = \frac{g\beta(T_w - T_\infty)y^3}{\nu^2} \quad (3.15)$$

Combining Equation 3.14 - 3.15 with the approximation of $g(Pr)$ proposed by Le Fevre [1956] yields the correlation for the local Nusselt number of a vertical isothermal plate shown in Equation 3.16.

$$Nu_{y,cor} = \left(\frac{Gr_y}{4} \right)^{1/4} \cdot \frac{0.75Pr^{1/2}}{\left(0.609 + 1.221Pr^{1/2} + 1.238Pr \right)^{1/4}} \quad (3.16)$$

A comparison of the data obtained by the present study and Ostrach [1952] is given in Figure 3.6.

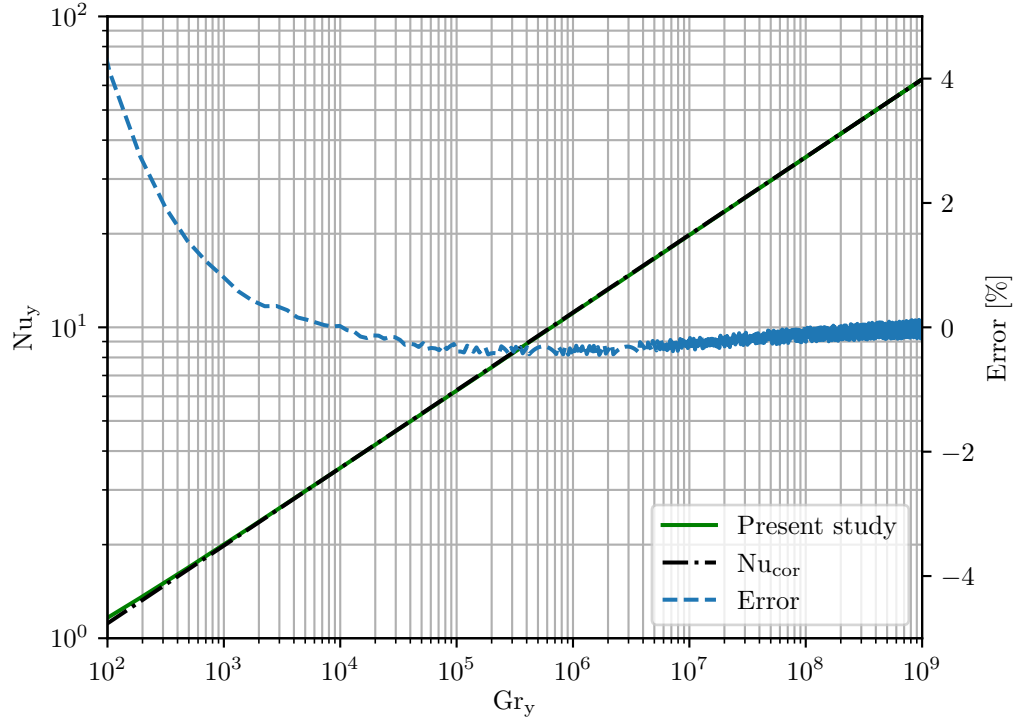


Figure 3.6: Comparison of the obtained numerical data for the vertical isothermal plate using a grid including 120000 cells with the correlation proposed by Ostrach [1952] (Equation 3.16). It is seen from the figure that the error is more pronounced at lower values of Gr_y , while the error approaches zero as Gr_y approaches 10^9 .

Here the green curve (—) is the results obtained from the present numerical simulations, while the black curve (— · —) represents the data obtained from the correlation outlined in Equation 3.16. Comparing the two curves it is evident that the numerical results obtained with the boundary conditions and grid shown in Figure 3.4(a) & (b) respectively, fits very well with the correlation data. The error between the two curves is more pronounced at lower values of Gr_y , where a 4.1 % difference is obtained at $Gr_y = 100$, and fades as Gr_y increases with a 0.06 % difference at $Gr_y = 10^9$.

Consequently, the validation together with the grid convergence study suggests that the boundary conditions used in Figure 3.4(a) resembles that of truly unconfined flow. It is thereby chosen to move on to the validation of natural convective channel flow using the same boundary conditions where possible.

3.4.2 Validation of natural convective channel flow

As shown in Section 3.4.1, the boundary conditions used for the vertical unconfined plate truly resembles that of unconfined flow as seen from the clear similarity of the plotted data in Figure 3.6. Due to the excellent fit, these boundary conditions are implemented in the channel domain where possible as shown in Figure 3.7.

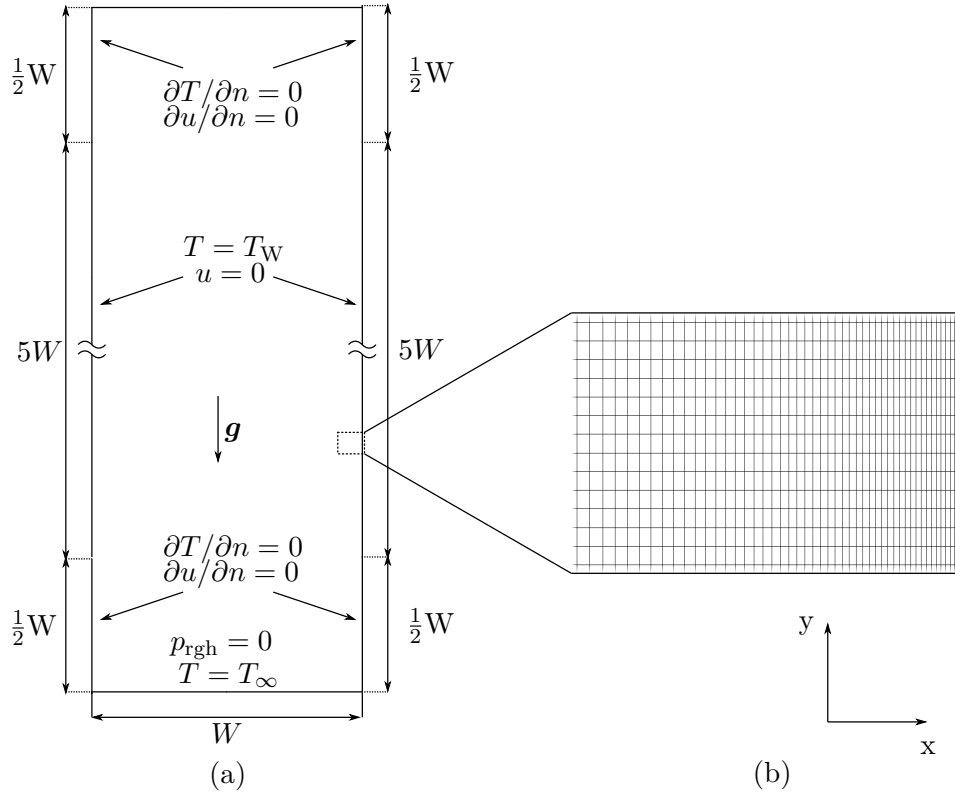


Figure 3.7: Here (a) shows the geometry and boundary conditions of the channel flow validation case, while (b) shows a cutout of the grid. The width of the channel is equivalent to the vertical plate domain shown in Figure 3.4, while the height of the heated channel section has been reduced to $5W$. The changes to the domain are introduced to ensure resemblance with the study conducted by Desrayaud and Fichera [2002]. The grading shown in (b) is similar to the one used for the vertical plate. The grading has an expansion ratio of 4 and is applied towards both walls.

As shown in Figure 3.7(a), the domain now includes identical walls on both sides, where again additional sections of length $1/2W$ are used to reduce the effect from the inlet- and outlet boundary condition, similar to the case shown previously in Section 3.4.1.

Comparing Figure 3.4 and Figure 3.7, it becomes apparent that the overall dimensions of the domain has changed. The channel has been shortened while keeping the width identical to the vertical plate domain. This is done in order to resemble the case shown in Desrayaud and Fichera [2002] which acts as the frame of reference in

the channel flow validation. The study presented in Desrayaud and Fichera [2002] utilizes a channel aspect ratio, denoted a ($=H/W$) equal to 5, which is implemented here as well. Furthermore, a channel Rayleigh number (Ra'_W) of 20000 is utilized and adopted in the present channel flow validation.

The procedures utilized to evaluate the validity of the boundary conditions in Section 3.4.1 are adopted in this section. Consequently, a grid convergence study is performed before moving on to the validation by comparison to the literature. Three different grids have been created, namely the coarse, medium and fine grids. Each refinement step increases the amount of cells in the domain by a factor of two, meaning that the amount of cells in the x- and y-direction are multiplied by a factor of $\sqrt{2}$. The data for the three grids (coarse, medium and fine) is outlined in Table 3.4.

Table 3.4: Grid convergence study data for the three different grids, namely the coarse-, medium- and fine grid where each step increases the total amount of cells by a factor of 2. The increase in cells is based on a multiplication of $\sqrt{2}$, in both the x-, and y-direction between each grid. Here \overline{Nu}_W is the surface averaged Nusselt number obtained by averaging the local Nusselt number (Nu_W) over the entire channel plate. The GCI values obtained for the coarse-medium and medium-fine grids are furthermore shown together with the evaluation of Equation 3.13.

Grid	Wall expansion rate	Cell count	\overline{Nu}_W
Coarse (128 x 166 x 1)	4	21248	7.1583
Medium (180 x 240 x 1)	4	43200	7.1150
Fine (255 x 336 x 1)	4	85680	7.0800
		coarse-medium	medium-fine
	GCI	$3.8 \cdot 10^{-2}$	$3.2 \cdot 10^{-2}$
	Equation 3.13	0.995	

In Table 3.4, the averaged Nusselt number \overline{Nu}_W is calculated as shown in Equation 3.10. From Table 3.4, it is seen that a compliance with the requirement stated in Equation 3.13 is achieved at relatively low values of the GCI, indicating a discretization error of approximately 3.2 % for the fine grid. In order to better represent the trend of the data, the averaged Nusselt number (\overline{Nu}_W) is plotted against the cell count in Figure 3.8.

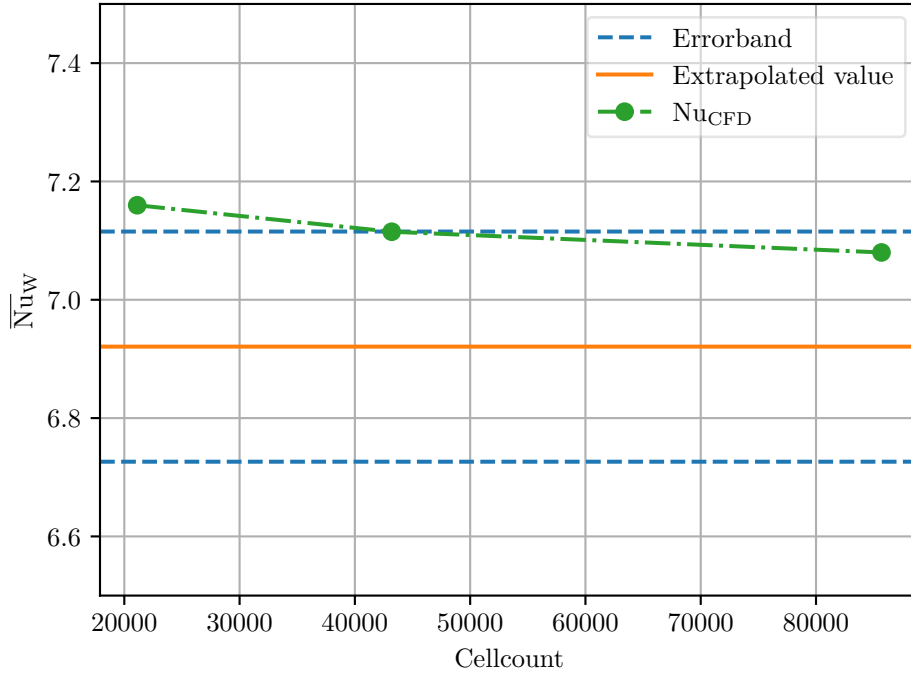


Figure 3.8: Development of the obtained results with grid refinement. Here the green curve (—·—) shows the average Nusselt number, while the blue (- - -) and orange (—) lines are indicators of the criteria of convergence. Here the blue lines show the error-bands, while the orange line shows the extrapolated final value with a grid of infinite refinement.

Here the green curve (—·—) represents the data obtained from the present CFD simulations, while the blue (- - -) and orange (—) curves represent the error-bands and extrapolated value respectively as described in Celik et al. [2008]. As the grid has proven to be grid independent, it is now possible to further validate the channel flow observations by comparing the obtained results with the literature. This is done by comparing the surface averaged results to the correlation proposed by Bar-Cohen and Rohsenow [1984], and the local wall Nusselt number presented by Desrayaud and Fichera [2002]. The correlation proposed by Bar-Cohen and Rohsenow [1984] is shown in Equation 3.17.

$$\overline{Nu}_w = \left(\frac{576}{Ra'_w{}^2} + \frac{2.873}{\sqrt{Ra'_w}} \right)^{-0.5} \quad (3.17)$$

Utilizing $Ra'_w = 20000$, Equation 3.17 yields $\overline{Nu}_w = 7.016$ which is approximately 1 % lower than the value obtained from the grid with 85680 cells. In order to further validate the channel flow case, local considerations of the Nusselt number are also

compared to the literature. This is done in order to assess the precision of the predicted values, as it is to be used as one of the key parameters in the comparison of the way channels. Here the local Nusselt number results obtained from $Y = 0$ to $Y = 5$ by the present numerical study and Desrayaud and Fichera [2002] is compared in Figure 3.9.

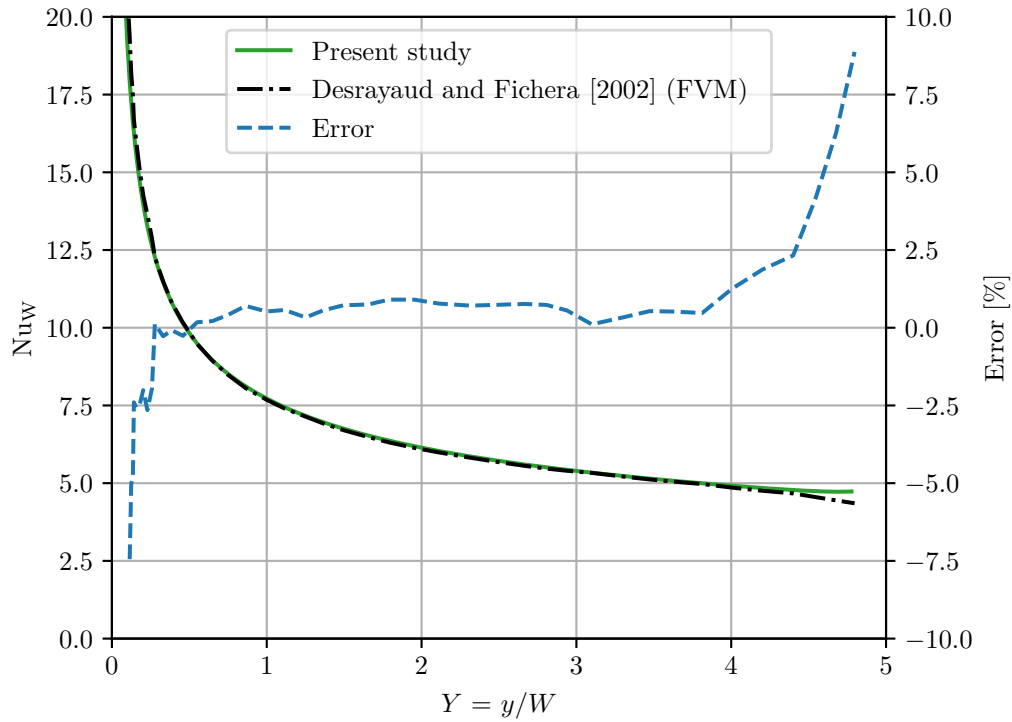


Figure 3.9: Comparison of the local Nusselt number, Nu_w , as a function of the dimensionless y -coordinate $Y = y/W$. All studies are conducted using the same aspect ratio of $a = 5$, and $Ra'_W = 2 \cdot 10^4$. The present study is compared to the numerical study presented by Desrayaud and Fichera [2002]. As the data is quite comparable, an additional curve is included in the figure showcasing the error between the two studies. As seen from the error it is clear the the error is more substantial at the beginning and end of the channel. The data obtained from Desrayaud and Fichera [2002] only includes comparable data until around $Y = 4.75$, where after the data seems to become unstable. Consequently, this comparison only include the value from $Y = 0$ to 4.75.

From Figure 3.9, it becomes evident that the data obtained in the present study and the data presented by Desrayaud and Fichera [2002] are in close agreement. Here the largest error in the local Nusselt number (Nu_w) is seen at the beginning ($Y \approx 0.05$) and end ($Y \approx 4.75$) of the channel, while it settles between zero and one percent between $Y \approx 0.4 - 4$. Both studies are conducted using comparable boundary conditions as described in Figure 3.7, with one exception being that the pressure has a specified value in the inlet compared to the outlet in Desrayaud and Fichera [2002]. Furthermore, the present study has implemented a vertical section before and after

the isothermal walls to reduce the effects of the inlet and outlet boundaries, which has not been included in Desrayaud and Fichera [2002]. Both studies are based on a finite volume solver utilizing similar algorithms for the pressure velocity coupling (SIMPLE in the present study and SIMPLER in Desrayaud and Fichera [2002]). Comparing the applied grids, it becomes evident that the present study has refined the domain with approximately 20 times the amount of cells reported in Desrayaud and Fichera [2002]. Consequently, the accuracy between this study and Desrayaud and Fichera [2002] is deemed adequate. This indicates that the numerical approach used in the present study is capable of replicating natural convective channel flow. Consequently, the grid with 85680 cells is adopted in the parametric study of the wavy channel sections in Chapter 4.

4 | Numerical parametric study

This chapter seeks to outline the procedures used and results obtained from the parametric study of natural convective flow in wavy channels. The range of the parametric parameters is outlined in Section 4.1 to give an overview regarding the size of the parametric study and to outline how the parameters affect the solution domain. The parametric study investigates the effects of changing the sine wave amplitude and wavelength of the geometry. Finally, the results of the parametric study are outlined in Section 4.2 and Section 4.3 giving an overview of the obtained data before recapping and discussing some further observations in Chapter 5.

4.1 Parametric geometry

The parametric investigation presented in this study primarily focus on deviations in the geometry of the channel. The geometry consists of a channel much like the one presented in Section 3.4.2, the shape of the walls is however changed to follow given sine waves. In this way, the geometry becomes parametric by changing the amplitude (h) and wavelength (L) of the sine wave used to represent the channel walls. A graphical representation of the parametric geometry and the range of each parameter is outlined in Figure 4.1 and Table 4.1 respectively.

As seen from Figure 4.1, the geometry consists of two identical sine wave walls which can be shifted by an amount ϕ as shown by the dotted line (- - -). The dotted line represents a phase shift of $\phi = \pi$, and is held constant at this value for the entire study. The sine wave height from peak to peak is $2h$, with a channel width of W given as the distance between the center lines of the respective sine waves as indicated by the dotted line (- · -). The channel aspect ratio is kept constant at $a = 5$ fixing the length of the channel in all simulations.

The range of each parameter, is outlined in Table 4.1, from which it is seen that a total of 21 simulations are conducted in the present parametric study. The parametric geometries used for the simulations are created by five different values of dimensionless amplitude (h/W), and five different values of the dimensionless wavelength (L/W). The four simulations not included represent the cases of $h/W = 0.00$ at all values of L/W . The dimensionless sine wave amplitude h/W is changed in increments of 0.02 starting from $h/W = 0.02$ with the maximum value corresponding to 8 % of the complete channel width, while L/W is changed in increments increasing the amount of wavelengths included from 3 ($L = 5/3W$) to 7 ($L = 5/7W$). All simulations are performed at a given value of $Ra'_W = 20000$ as presented in the validation of natural convective channel flow in Section 3.4.2.

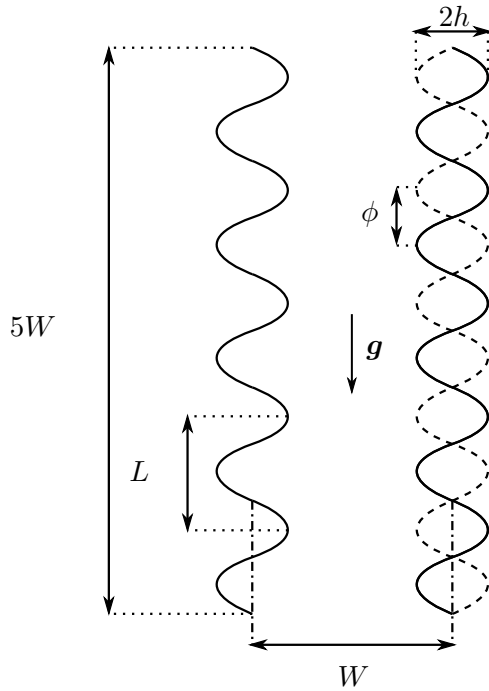


Figure 4.1: Here ϕ is the phase shift of the sine wave used to form the channel walls. The phase shift is applied to the right wall, with a phase shift of zero corresponding to identical channel walls. Depicted in the figure is a phase shift of π , as shown by the dotted line (- - -). Furthermore, h represents the amplitude of the sine wave, W represents the channel width taken as the distance between the center lines of the sine waves as shown by the dotted line (-·-·-) and L represents the wavelength of the sine wave. The aspect ratio, denoted a , of the channel is held constant at 5.

Parametric study	
Parameter	Range
ϕ	π
h/W	0.02, 0.04, 0.06, 0.08
Ra'_W	20000
L/W	5/3, 5/4, 5/5, 5/6, 5/7

Table 4.1: Different parameters used in the parametric studies. Here ϕ represents the phase shift, h/W the dimensionless amplitude, W the channel width, L/W the dimensionless wavelength and Ra'_W the channel Rayleigh number. The ranges of each parameter is given in the second column of this table, where a combination of each parameter is used in the parametric studies. Consequently, 21 different simulations are performed in total for the parametric studies.

4.2 Flow and temperature considerations

In this section the flow- and temperature field from the parametric study investigating h/W and L/W is presented and discussed. To give an understanding of how the flow changes with h/W , examples of the velocity and temperature fields are shown in Figure 4.2. The cases in Figure 4.2 represent channels with $h/W = 0.02$ and 0.08 when $L/W = 5/5$, as these represent the extreme cases of h/W values resulting in relatively large differences in the flow and temperature fields. The geometry shown in Figure 4.2, includes the complete heated channel section from $X = 0$ to 1 and $Y = 0$ to 5. The left plots in Figure 4.2 show the dimensionless velocity U' first for $h/W = 0.02$ and then 0.08 , while the right plots show the dimensionless temperature

θ in the same order.

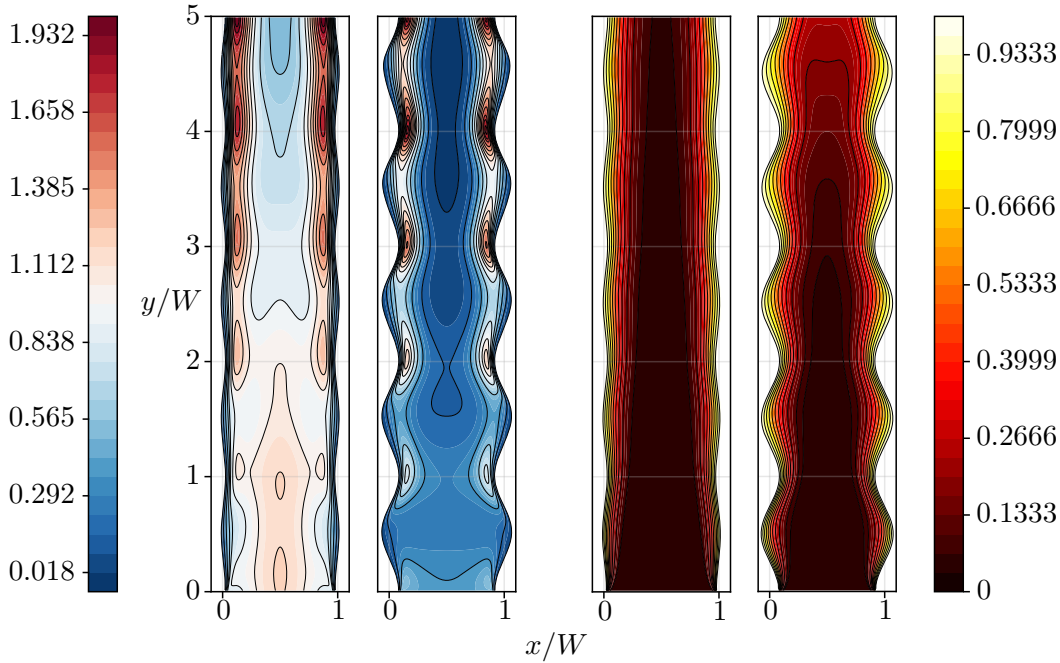


Figure 4.2: The effect of changing the dimensionless sine wave amplitude h/W on the dimensionless velocity field $\mathbf{U}' = \mathbf{U}|\mathbf{U}|/(|\mathbf{g}|\beta(T_w - T_\infty))$ and dimensionless temperature field $\theta = (T - T_\infty)/(T_w - T_\infty)$ at $Ra'_W = 20000$. The blue-red contours (left) are dimensionless velocity and black-red-yellow contours (right) are dimensionless temperature.

From the left plots in Figure 4.2 it is observed that the velocity increases along the heated wall as expected. The repeating acceleration and deceleration of the flow becomes more apparent as h/W increases, which can also be seen by the high velocity zones being more centered at the narrow parts of the channel in $h/W = 0.08$. Consequently, the low velocity zones become more prominent as h/W increases. It is thereby expected that the local heat transfer from these areas decreases due to the increase in temperature in the relatively slow fluid close to the wall. A higher temperature in the low velocity zones reduces the temperature gradient from the wall into the fluid, which in turn lowers Nu_W .

This behaviour is further substantiated by the plots to the right in Figure 4.2, where a bright yellow color showcases $\theta \approx 1$. Furthermore, it is observed from the dimensionless temperature plots that the temperature in the outlet of the channel rises as h/W increases. This behaviour suggests that the fluid momentum is lowered through the channel due to the increased flow obstruction and decreased gradient at the wall.

Finally, it is seen from Figure 4.2, that the flow is symmetric around the vertical center axis of the channel. This is especially noticeable in the temperature contours, where each contour follow the channel geometry. As the contours are symmetric, it

is expected that the local heat transfer coefficient of both walls has the same shape, which will be investigated further in Section 4.3. For now the symmetric behaviour of the channel is utilized to reduce the size of the plots to include half the channel from $y/W = 0.5$ to 1. As an example of how the flow changes with L/W , the dimensionless velocity- and temperature contours of the channels with $L/W = 5/3$, $5/4$, $5/6$ and $5/7$ are depicted in Figure 4.3 and 4.4 respectively. The setup of the figure is similar to Figure 4.2, where the channel with $h/W = 0.02$ is to the left while the channel with $h/W = 0.08$ is to the right in each L/W pair marked at the top of the figure. These are chosen to show the largest differences in the velocity- and temperature field, where the channels with $h/W = 0.04$ and 0.06 lie in between.

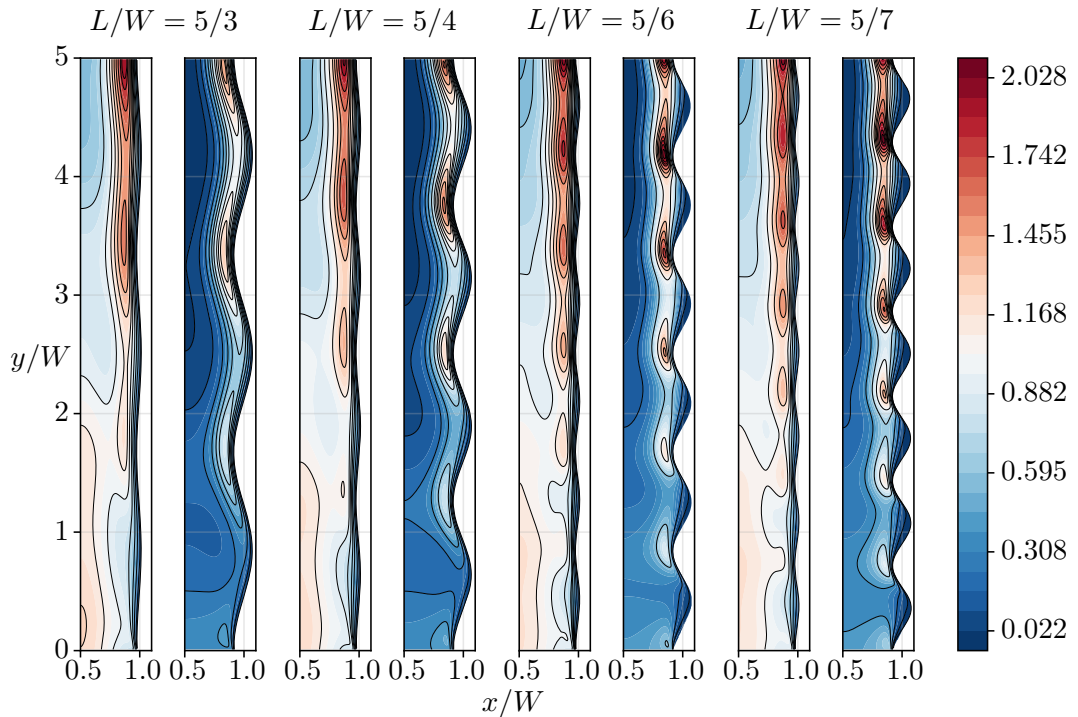


Figure 4.3: Plots of the dimensionless velocity U' at different values of L/W . The plots shown include geometries with $h/W = 0.02$ and 0.08 , where the geometry with h/W is located to the left in each L/W pair.

As seen from Figure 4.3, there are some substantial differences in the velocity fields when comparing different combinations of L/W and h/W . Comparing the different L/W contours it is apparent that there are only minor differences in the flow field. Common to all is a velocity increase at the wall, due to the buoyancy force, with a decrease in velocity in the middle of the channel. The highest value of U' is obtained at $L/W = 5/7$ and $h/W = 0.08$, which suggests that this setup has the highest peak in heat transfer coefficients out of all the similar cases at different values of L/W . As mentioned earlier, the velocity inside the right facing peaks of the wall is

of lower magnitude compared to the bulk flow. In fact, it is noticed that the lowest increment in the velocity colorbar has a negative value. It is furthermore noticed that this contour level is not present in the cases with $h/W = 0.02$ for all values of L/W . The contour level does however appear in the channels with $h/W = 0.08$ at all levels of L/W . The area of the negative contour level increases with decreasing L/W , and reaches a maximum at $L/W = 5/7$. It is furthermore seen from the figure that the size of the contour inside the right facing peaks increases with y/W caused by the velocity increase due to the heating of the channel flow. As a consequence of this, recirculation zones are formed in inside the low velocity zones from the middle to the end of the channel in the case of $L/W = 5/7$ and $5/6$ when $h/W = 0.08$. This behaviour might be a possible indication that the surface averaged heat transfer coefficient of the channels decrease when h/W and L/W increases and decreases respectively.

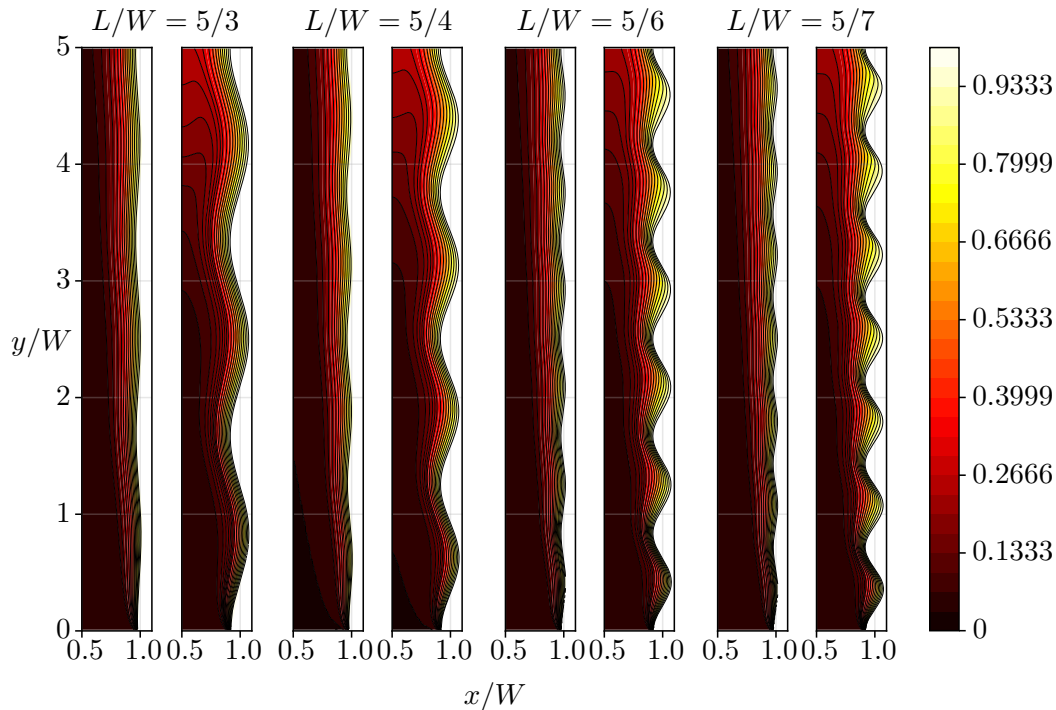


Figure 4.4: Plots of the dimensionless temperature θ at different values of L/W . The plots shown include geometries with $h/W = 0.02$ and 0.08 , where the geometry with h/W is located to the left in each L/W pair.

Moving on to the dimensionless temperature contours shown in Figure 4.4, it is observed by comparison that the behaviour of the temperature field follows that of the velocity field relatively well. Comparing the results obtained for $h/W = 0.02$ and $h/W = 0.08$ for all L/W pairs does again reveal a substantial difference in the temperature field. Here it is observed that in all cases, the temperature field in $h/W = 0.02$ becomes less developed across the channel width. This is directly

coupled to the observations in the velocity fields, where the channels with $h/W = 0.08$ all have relatively low bulk flow velocities in the channel compared to the $h/W = 0.02$ channels. Lower bulk fluid velocities does in this way decrease the heat transfer coefficients due to smaller temperature gradients across the channel. With these observations in mind, the next section seeks to outline the behaviour of the heat transfer of the channels by comparing both the local Nusselt numbers and surface averaged Nusselt numbers between different channel setups.

4.3 Evaluation of the wavy channel heat transfer performance

This section seeks to evaluate the heat transfer performance of the varying parametric channels through the development in the local and surface averaged values of the channel Nusselt number. The geometry is varied according to different values of L/W and h/W as described in Section 4.1, with five different values of L/W and five values of h/W .

4.3.1 Evaluation of the heat transfer coefficient

To show how the heat transfer develops through the channel as the geometry changes due to the variations in L/W and h/W , plots of the local Nusselt number (Nu_W) are shown for $L/W = 5/3, 5/4, 5/6$ and $5/7$ in Figure 4.5a - 4.5e respectively.

As seen from Figure 4.5a - 4.5e, the local heat transfer changes quite substantially as both L/W and h/W changes. The data given as $h/W = 0.00$ represents the vertical channel at $Ra'_W = 20000$, which acts as the frame of reference. Comparing all setups, it is apparent that the local Nusselt number (Nu_W) follows the geometry of the channel, rising and decreasing as the channel converges towards- and diverges from the channel center respectively. The amount of peaks does in this way increase with decreasing L/W , as seen by comparison of Figure 4.5a-4.5e. The decrease and increase in Nu_W can be explained by the before mentioned low velocity zones due to the acceleration and deceleration of the flow caused by the geometry. In this way larger and more peaks are observed as h/W increases and L/W decreases. The low peaks are thereby explained by the decreased temperature gradient due to the increased temperature in these zones, while the opposite is the case for the peak locations. Comparing $L/W = 5/3$ with $L/W = 5/7$, it is clear that the peaks when $L/W = 5/7$ are relatively large, with the subsequent lows being of the same magnitude. In this way, the difference in heat transfer between these cases might not be as large as it appears. Comparing the different L/W channels with the frame of reference ($h/W = 0.00$ / vertical channel), it is clear that some of the channels seem to oscillate around the data obtained for the vertical channel, while others oscillate around a lower magnitude value.

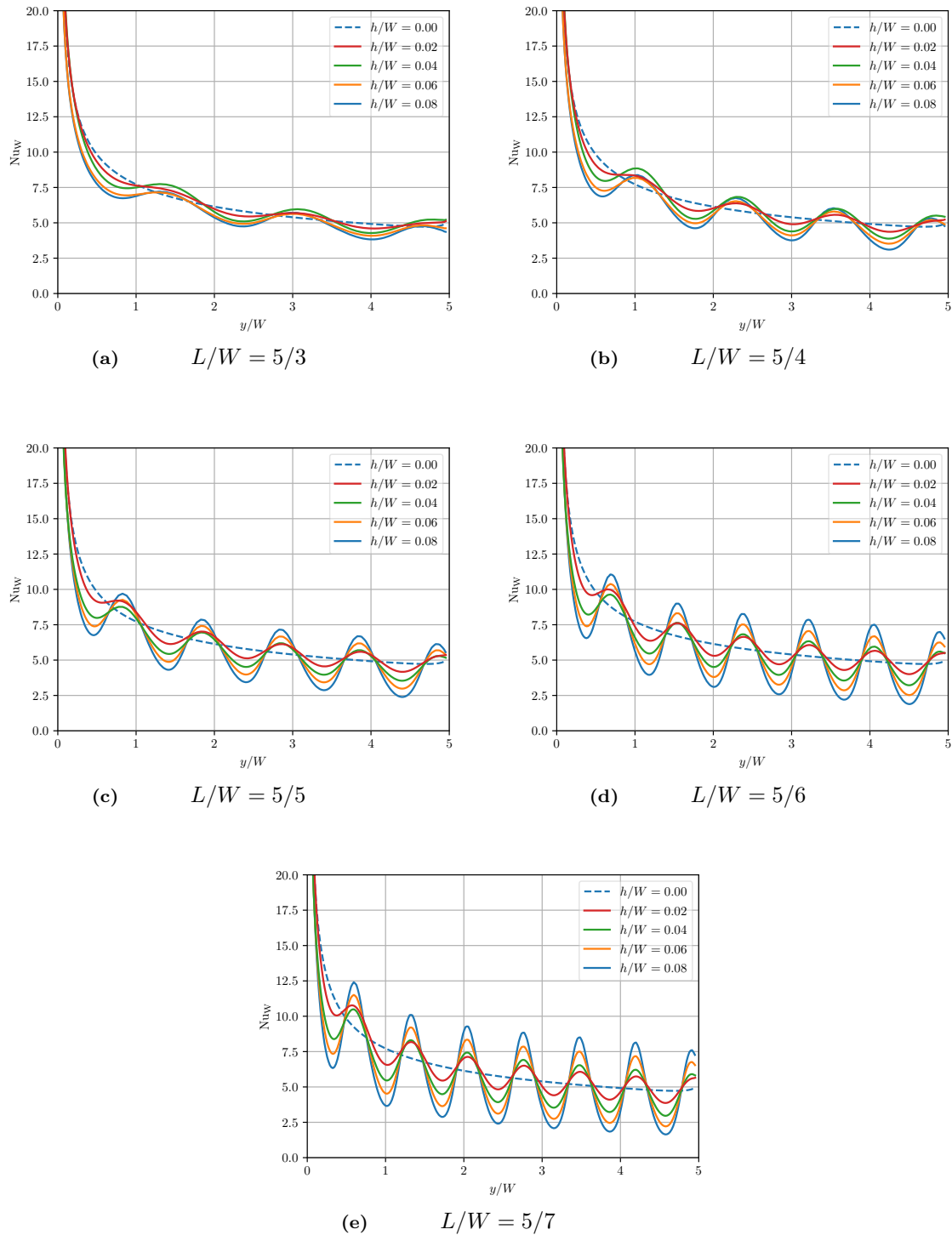


Figure 4.5: The local channel Nusselt number (Nu_W) for different channel setups. Here (a) shows Nu_W for a channel with $L/W = 5/3$, (b) shows Nu_W for a channel with $L/W = 5/4$, (c) shows Nu_W for a channel with $L/W = 5/5$, (d) shows Nu_W for a channel with $L/W = 5/6$ and (e) shows Nu_W for a channel with $L/W = 5/7$. Each L/W plot includes 5 different h/W setups, namely $h/W = 0, 0.02, 0.04, 0.06$ and 0.08 .

In this way, it is expected that the overall heat transfer coefficient of the channel will either be in the same magnitude as the reference case or lower than the reference case. An overview with respect to the overall heat transfer coefficient of the channel, compared to the vertical channel is given in Figure 4.6. The contours show the ratio between the surface averaged Nusselt number obtained for the wavy and vertical channel (VC). The surface averaged Nusselt number ratio \overline{Nu}_{ratio} is given in Equation 4.1.

$$\overline{Nu}_{ratio} = \frac{\overline{Nu}_W}{\overline{Nu}_{W,VC}} \quad (4.1)$$

Here (\overline{Nu}_W) is the surface averaged Nusselt number of the wavy channels, and ($\overline{Nu}_{W,VC}$) represent a similar value for the vertical channel.

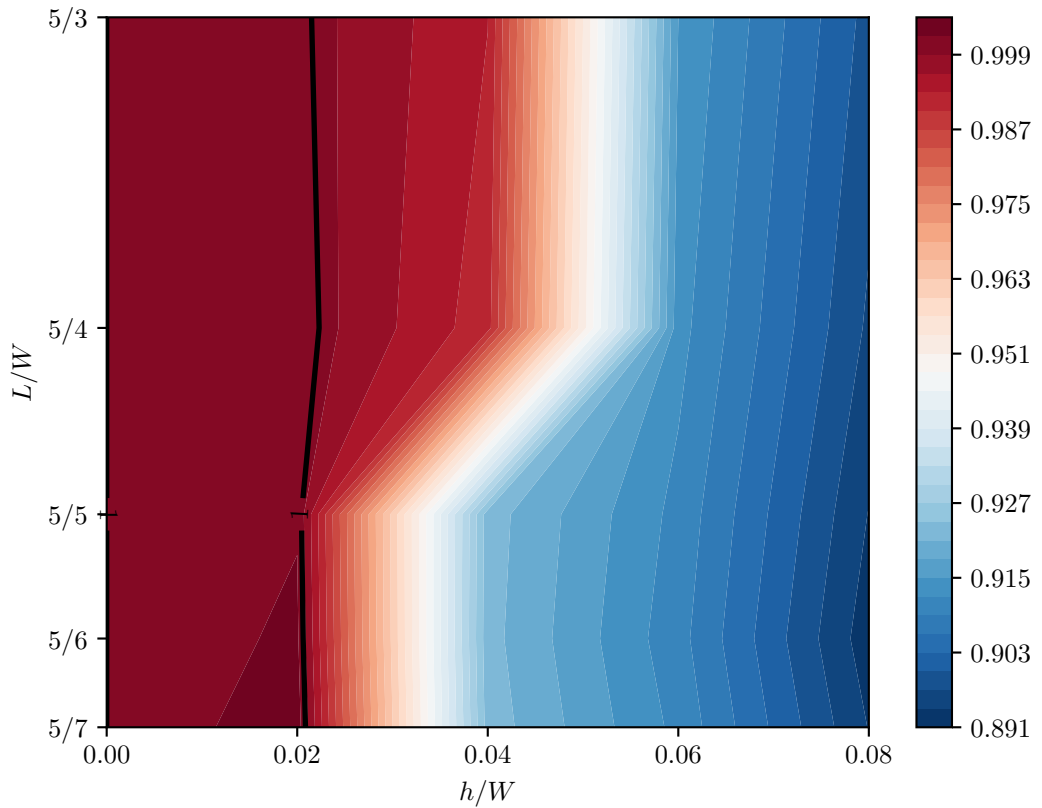


Figure 4.6: Contour plot showing the changes in the averaged channel Nusselt number ratio (\overline{Nu}_{ratio}) as a function of variations in h/W and L/W .

It is observed from Figure 4.6 that the channels with $h/W = 0.02$ for all values of

L/W seem to increase the average heat transfer coefficient of the channel slightly compared to the vertical channel ($h/W = 0.00$). This is indicated by the solid line indicating a ratio value of 1, where a darker shade of red indicates $\overline{Nu}_{\text{ratio}} > 1$. All other setups seem to decrease the overall heat transfer coefficient ratio, with the largest decrease amounting to approximately 11 % obtained from the channel with $L/W = 5/6$ and $h/W = 0.08$. Referring to the findings in the local Nusselt number, which were difficult to distinguish exactly, it has become apparent that the heat transfer coefficient of channels with a combination of moderate to high h/W values at all values of L/W seem to worsen the heat transfer coefficient. However, it should be given attention that this does not take into account the increase in area associated with these channels. Consequently, Section 4.3.2 seeks to investigate the overall heat transfer of the channel by taking into account the area increase as well.

4.3.2 Area increase due to wavy channel walls

As discussed in Bhavnani and Bergles [1991], the wavy plate geometry has the potential to increase heat transfer based on projected area when compared to a vertical plate. Referring to the results presented in Chapter 4, it is clear that most of the channels investigated in the present study decreases the overall heat transfer coefficient compared to the vertical channel. The heat transfer is decreased as much as 11 % compared to the vertical channel when $h/W = 0.08$ at $L/W = 5/6$ as shown in Figure 4.6. In order to take into account the area increase, a heat transfer performance parameter Q_{ratio} has been introduced. The performance parameter is given as the product between the Area- and surface averaged Nusselt number ratios, as shown in Equation 4.2.

$$Q_{\text{ratio}} = \overline{Nu}_{\text{ratio}} \cdot A_{\text{ratio}} = \frac{\overline{Nu}_W}{\overline{Nu}_{W,VC}} \cdot \frac{A}{A_{VC}} \quad (4.2)$$

Here A is the wavy channel area and A_{VC} is the vertical channel area. Figure 4.7 shows the relative increase in area between the wavy geometries and the vertical channel per wall as a function of the variation in L/W and h/W . As observed from Figure 4.7, the area increase is greatest when the dimensionless wavelength and dimensionless amplitude of the wavy channel is greatest. When $L/W = 5/7$ and $h/W = 0.08$ an increase in area of approximately 11 % is obtained per wall. The area increase then diminishes as L/W and h/W decreases.

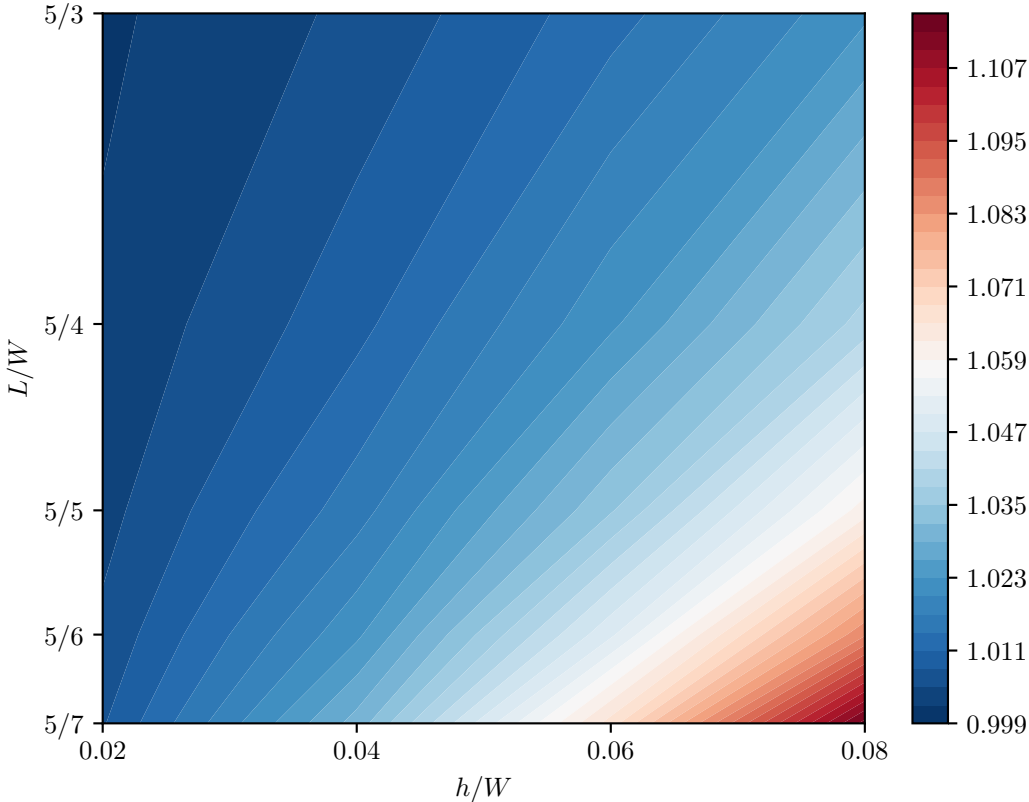


Figure 4.7: Contour plot of the area ratio for the wavy geometry to the vertical channel for one wall.

With these values in mind, and using the definition of the heat transfer performance parameter in Equation 4.2, the data shown in Figure 4.8 is obtained.

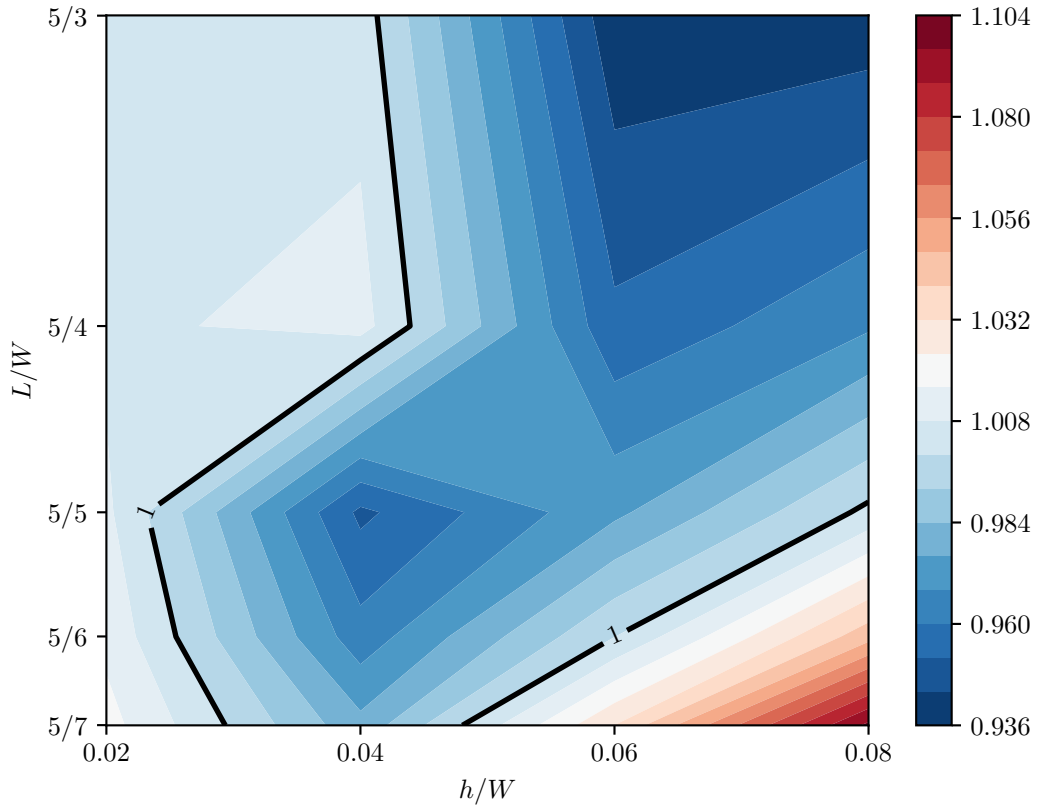


Figure 4.8: Contour plot of Q_{ratio} as a function of L/W and h/W . Here the different values of L/W and h/W are utilized to obtain values of A_{ratio} and $\text{Nu}_{W,\text{ratio}}$.

As seen from Figure 4.8, the values of Q_{ratio} above 1 seem to occur at specific combinations of L/W and h/W . For convenience a recap of the channel combination with a ratio above one is given in Table 4.2.

Table 4.2: Recap of the channel combination of L/W and h/W yielding a heat transfer ratio, Q_{ratio} , above 1.

L/W	h/W
5/7	0.02, 0.06, 0.08
5/6	0.02, 0.08
5/5	0.02, 0.08
5/4	0.02, 0.04
5/3	0.02, 0.04

As seen from a combination of Figure 4.8 and Table 4.2 there is no clear pattern

in what combinations of L/W and h/W yields values of Q_{ratio} above 1. Comparing Figure 4.8 (Q_{ratio}) with Figure 4.6 ($\overline{Nu}_{\text{ratio}}$) and Figure 4.7 (A_{ratio}) it is observed that the area has a large influence on the overall heat transfer in the channel. As previously stated, it is only in some of the wavy channels that an increase in \overline{Nu}_W is observed, but with a large increase in area some of the channels now have a larger overall heat transfer ratio. This suggests that the increased area of the wavy channel does in fact increase the overall heat transfer of the channel based on projected area as stated for wavy plates in Bhavnani and Bergles [1991]. The tendency seems to favor relatively low values of L/W with large values of h/W . Consequently, this suggests that a further decrease in L/W and increase in h/W might increase the heat transfer of the channel beyond what is observed in the present study.

This concludes the result chapter of the parametric study, a short summary of the findings is given in Chapter 5, together with a discussion.

5 | Summary and discussion of results

Through the numerical investigation it is evident that the introduction of wavy channel walls yield mixed results depending upon the geometrical setup of the channel. Investigating the local Nusselt number of the channel, it is found that the peaks in Nu_W follow the geometry and increase with a reduction in wavelength (L/W) or an increase in amplitude (h/W) of the sine wave. This can be explained by the rate at which the channel expands, which increases with increasing h/W and decreasing L/W . This introduced more rapid deceleration and acceleration of the flow, yielding more extreme peaks in the velocity field, and consequently the local heat transfer coefficient.

The wavy channels are found to generally decrease the surface averaged Nusselt number (\overline{Nu}_w) of the channel, with larger decreases occurring as h/W increases. Additionally, it is found that the reduction in \overline{Nu}_w is somewhat delayed at larger values of L/W . Here the channels with $L/W = 5/3$ and $5/4$ seem to be able to perform nearly as well as the vertical channel when $h/W = 0.04$, which is not the case for channels with $L/W = 5/5$, $5/6$ and $5/7$. From the velocity fields it has been observed that recirculation zones are present at three combinations of h/W and L/W , namely when:

- $h/W = 0.06, 0.08$ and $L/W = 5/7$
- $h/W = 0.08$ and $L/W = 5/6$

These channels all represent some of the lowest surface averaged heat transfer coefficients, which might be explained by the recirculation zones. Finally, it is observed that the channels with $h/W = 0.02$ seems to perform slightly better than the vertical channel in terms of \overline{Nu}_w at every value of L/W , which seems very promising taking into account the increase in area has not been taken into account.

Taking the area gained by lowering the wavelength and increasing the amplitude into account, the total heat transfer shows a different behaviour than the Nusselt number ratio. Taking the area increase into account, it is found that several of the channels outperform the vertical channel. It is generally found that larger increases in the heat transfer performance parameter Q_{ratio} is observed at high values of h/W and low values of L/W . The channel that performs the best in the simulated range of variables is the channel with $h/W = 0.08$ and $L/W = 5/7$. This channel has one of the lowest values of \overline{Nu}_w , but such a large increase in area, that it outweighs the reduction in \overline{Nu}_w , thereby obtaining $Q_{ratio} = 1.1$

5.1 Construction of a wavy channel array

Until now all considerations of the channel have been with a diverging beginning, which introduces a deceleration of the flow. This is especially noticeable in the local Nusselt number plots, where a large drop compared to the vertical channel occurs in the beginning of the channel. If these channels are used to construct an array, it is evident that some area is lost as shown by the gray areas in Figure 5.1. The lost area decreases the overall heat transfer of the array by reducing the effective flow area of the array. If the channel on the other hand is allowed to consist of alternating diverging/converging channels, as shown in Figure 5.2, the area loss is none existent. Consequently, this section seeks to investigate the heat transfer performance of a channel with a converging beginning at $Ra'_W = 20000$, $L/W = 5/5$ under the entire range of h/W .

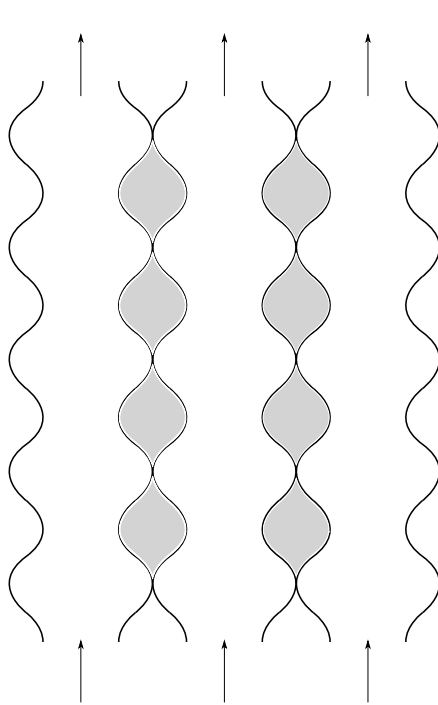


Figure 5.1: Array of wavy channel walls formed by diverging channels. Here the gray areas in the figures represent the lost area. Channels are indicated by the arrows which indicates the flow passages.

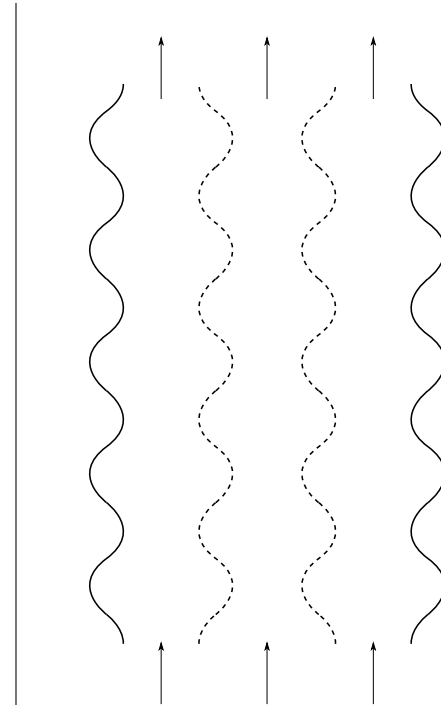


Figure 5.2: Array of wavy channel walls formed by a combination of alternating diverging/converging channels. Here no area is lost due to the construction of the channel. Channels are indicated by the arrows which indicates the flow passages.

In order to evaluate the heat transfer performance of the channel with a converging beginning, a setup similar to the one presented in Section 3.4.2 is utilized for the domain shown by the dotted line in Figure 5.2. In order to showcase the differences in local heat transfer between the channel with a converging and diverging beginning,

the local Nusselt number is depicted in Figure 5.3. Here the blue solid and blue dashed lines represent two frames of references, namely the channel with a diverging beginning and the vertical channel respectively. The diverging case with $h/W = 0.08$ is chosen as it is expected to see a larger difference in local Nusselt number as h/W increases. All other lines represent a channel with a converging beginning at different h/W values.

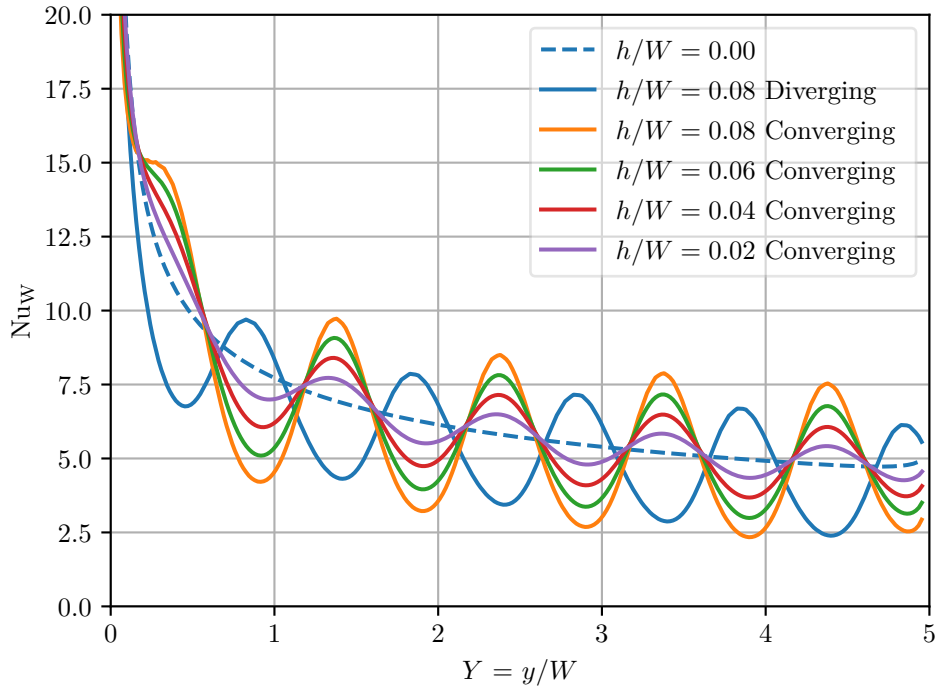


Figure 5.3: Local Nusselt number (Nu_W) with $Ra'_W = 20000$. The data is presented for the entire range of h/W , and compared to the vertical channel ($h/W = 0.00$) and the channel with a diverging beginning when $h/W = 0.08$. The simulations are all performed at $L/W = 5/5$. The labels converging and diverging refer to how the beginning of the channel is shaped.

From Figure 5.3 it is clear that the converging channel performs better in the beginning of the channel. This is also expected as the flow will accelerate instead of decelerate as seen in the diverging case. The local Nusselt number (Nu_W) follows the flow and oscillates opposite to the diverging channel, with larger difference between the peaks. This large value of Nu_W in the beginning of the channel contributes substantially to the surface averaged Nusselt number (\overline{Nu}_W), as the channels are relatively short. The Nusselt number ratio \overline{Nu}_{ratio} , and the performance parameter Q_{ratio} for the channels with a converging/diverging beginning are given in Table 5.1.

Table 5.1: Values of the Nusselt number- and performance parameter, given as \overline{Nu}_{ratio} and Q_{ratio} respectively, for all cases of h/W . The values are furthermore divided into the channel with a diverging/converging beginning in order to show the differences between the geometries. Both ratios are given with respect to the reference vertical channel. The simulations are conducted at $Ra'_W = 20000$, and $L/W = 5/5$.

$\overline{Nu}_{W,ratio}$					
h/W	0	0.02	0.04	0.06	0.08
Diverging	1	1.002	0.922	0.911	0.894
Converging	1	0.997	0.983	0.962	0.935
Q_{ratio}					
h/W	0	0.02	0.04	0.06	0.08
Diverging	1	1.009	0.950	0.974	1.002
Converging	1	1.005	1.013	1.023	1.048

Based on the data from Table 5.1, it seems as if the converging channels perform better measured on the Nusselt number for relatively short channels, with the exception of $h/W = 0.02$. As an example, \overline{Nu}_{ratio} has been increased by approximately 4.4 % between the diverging/converging channels at $h/W = 0.08$. Consequently, it is also expected that Q_{ratio} of the converging channel outperforms that of the diverging channel. This behaviour is substantiated by the data shown in Table 5.1, where all converging channels obtain a heat transfer ratio Q_{ratio} above 1. This indicates that the alternating diverging/converging channel array will increase the overall heat transfer compared to the array consisting of only diverging channels. It is thereby recommended that this array setup should be implemented and further tested in a prototype.

6 | Conclusions

In this work, changes observed in flow phenomena and heat transfer due to the implementation of wavy channel walls in natural convection has been investigated. The wavy channels were created by changing two geometric parameters, namely the dimensionless amplitude (h/W) and wavelength (L/W). The CFD simulations were performed in OpenFOAM using DNS and validated by correlations and other similar studies in the literature. A script was developed in Python to create the wavy geometry effectively before meshing was conducted in blockMesh. The computational domain consists of an isothermal wavy channel at an aspect ratio of five with additional vertical adiabatic channels at the inlet and outlet. The additional channel segments are implemented to decrease the effects from the inlet and outlet boundary conditions and to increase stability of the simulations. The above mentioned procedures are used to conduct a parametric study where the two dimensionless geometrical parameters used to construct the channels were varied. The parameters are changed in increments, where a range from $5/7$ to $5/3$ is used for L/W , which includes 7 to 3 wavelengths over the entire channel, while h/W is changed between 0 and 0.08 in increments of 0.02. The parametric study includes 21 simulations in total.

It is found from the study that recirculation zones are present when $h/W = 0.06$ and 0.08 at $L/W = 5/7$ and when $h/W = 0.08$ at $L/W = 5/6$. These recirculation zones occur as the rate of expansion due to the high amplitude and low wavelength makes it difficult for the flow to creep along the walls. The recirculation zones furthermore contribute to the increased thickness of the temperature boundary layer reducing the temperature gradient, and thereby heat transfer coefficient adjacent to the walls.

In general it is found that an increase in h/W at $Ra'_W = 20000$ entails a decrease in the surface averaged Nusselt number compared to the vertical channel, while a very slight increase is observed at $h/W = 0.02$. Additionally, it is found that the wavelength of the sine wave drastically changes the local heat transfer coefficient, with greater magnitude peaks being observed as L/W decreases. The change in wavelength does however not increase the average heat transfer coefficient of the channel substantially, with the largest increase being 0.35 % at $h/W = 0.02$ and $L/W = 5/7$. The largest decrease of approximately 10.8 % is obtained at $h/W = 0.08$ and $L/W = 5/6$. The wavelength does however contribute greatly to the increase in area, where an increase in area compared to the vertical channel of approximately 22.8 % is observed at $L/W = 5/7$ and $h/W = 0.08$. In order to evaluate the heat transfer of the channels, the performance parameter Q_{ratio} is introduced. Here values of Q_{ratio} above one suggests that the overall heat transfer of the channel based on projected area is greater compared to the vertical channel. Consequently, it can be concluded that the channels with $h/W = 0.08$ at $L/W = 5/7$, $5/6$ and $5/5$ all obtain a performance ratio compared to the vertical channel above one. The large increase in area does in this way outweigh the decrease in surface averaged heat transfer co-

efficient resulting in an increase in the total heat transfer of the channel.

As the channels investigated in the parametric study all follow a diverging pattern at the beginning of the channel, possibly reducing the overall surface area of the heat sink array, the channel with a converging beginning has been studied. Here it can be concluded that the channel with a converging beginning has increased the overall heat transfer coefficient of the channel at all values of h/W except $h/W = 0.02$ where it is within 0.5 % of its diverging counterpart, for relatively short channels.

A | Literature review

Field of investigation	Method	Findings	Reference
<ul style="list-style-type: none"> Natural convection from an inline array of rectangular heated protrusions mounted on a vertical surface in water Component power dissipation levels varied from 0.2 W - 1.5 W Flow visualization 	<p>Experimental temperature measurements with thermocouples</p> <p>Flow visualization done with a 8 mW helium-neon laser sheet, particles in flow and a camera.</p>	<p>It was found that the upper side of the rectangular protrusions was the warmest, while the side was the coldest</p> <p>Flow visualizations revealed the boundary layer and boundary layer buildup for the specific geometry investigated.</p>	[Joshi et al., 1989]
<ul style="list-style-type: none"> Mixed convection along a wavy surface 	Numerical investigation	<p>The wall heat transfer rate is found to vary accordingly to the slope of the surface</p> <p>found harmonics in the local nusselt number with a base frequency according to the wavy surface.</p> <p>Averaged values of nusselt number found to be universally lower than that of the flat surface</p>	[Ghosh Moulic and Yao, 1989]
<ul style="list-style-type: none"> Free-convection flat vertical plates 	Experimentally and based on calculations	<p>Determined Grashof number to be key in determining type of flow. and obtained correlation between Nusselt number and Grashof Number.</p>	[Ostrach, 1952]
<ul style="list-style-type: none"> Heat transfer by natural convection with perforated fins Varies fin spacing, perforation angle, perforation diameter and pitch of perforation 	experimental measurements	<p>4mm perforation diameter and 45 degree geometry of perforation found to be optimum for heat transfer.</p> <p>Includes a literature review</p>	[Pankaj et al., 2018]
<ul style="list-style-type: none"> Fully-developed inline square pin fin heat exchanger Varies Grashof number and geometrical pitch between 1.5 and 3 	2 dimensional numerical simulation using periodic boundary conditions and the MAC algorithm	<p>Flow becomes unsteady above a critical Grashof number</p> <p>Critical Grashof number decreases with increasing fin spacing</p> <p>Nusselt number found to increase with increasing Grashof number for a specific geometry, whereas nusselt number decreases for an increase in pitch with constant Grashof.</p>	[Saha and Chanda, 2019]

Field of investigation	Method	Findings	Reference
<ul style="list-style-type: none"> Looks into forced convection pin fin heat exchangers with circular, cone and hydrofoil shaped vs. plate fins Natural convection with one heated ribbed surface and an opposing unheated smooth surface. Fin spacing and rayleigh number was varied Natural convection with low thermal conductivity square ribs in a vertical channel Number of protrusions was varied together with channel aspect ratio Forced convective heat transfer in periodic wavy passages Natural convection from pin fin arrays 	<p>Numerical simulation with natural convection and radiation neglected</p> <p>Experimental investigation</p> <p>Experimental investigation</p> <p>numerical simulation probably 2D</p> <p>Experimental and empirical modelling</p> <p>Experimental investigation using both uniform wall temperature and uniform wall heat flux</p> <p>Experiments compared with correlations</p>	<p>All 3 types of pin finned heat exchangers outperformed plate fin with 1.6-2 times</p> <p>Found the ripped channel performed worse than the smooth based on average heat transfer</p> <p>For a very large fin spacing (40% of channel height) a fin with 1 protrusion was comparable to the flat plate in terms of heat transfer</p> <p>Increases in heat transfer was only achieved locally for the range of parameters investigated</p> <p>Wavy fins performed about the same in the laminar regime as flat plates and outperformed the flat plates by a factor of 2-2.5 in the wavy/transitional regime</p> <p>Most influential parameter is the ratio of the pin diameter and the center to center spacing</p> <p>It is found that the average Nu is about 10-13 % higher in smooth channels compared to ribbed channels in natural convection. The probable reason for the decreased heat transfer is the low velocity regions in the near rib space.</p> <p>It is found that the schlieren and holographic experiments correlate well with data obtained from the literature</p> <p>It is found that all ribs have high heat transfer at the leading edge and decreased heat transfer at the trailing edge</p>	<p>[Sakanova and Tseng, 2018]</p> <p>[Tanda, 1997]</p> <p>[Tanda, 2008]</p> <p>[Wang and Vanka, 1995]</p> <p>[Zografos and Sundland, 1990]</p> <p>[Acharya and Mehrotra, 1993]</p> <p>[Ambrosini and Tanda, 2005]</p>
<ul style="list-style-type: none"> Natural convection heat transfer in vertical channels with and without roughening ribs Investigated experimentally via different optical techniques 			

Field of investigation	Method	Findings	Reference
<ul style="list-style-type: none"> Natural convection of vertical heated plates with and without ribs Measurements of heat transfer coefficients over the plate Heat transfer by natural convection inside asymmetrically heated, vertical, ribbed channels with water as coolant 	Experimental	<p>The introduction of ribs increase the local heat transfer coefficient substantially at the rib locations</p> <p>The increase in heat transfer is approximately 9.2 % for aluminium fins and 6.3 % for plexiglas ribs</p>	[Aydin, 1997]
<ul style="list-style-type: none"> Investigation of natural convection heat transfer from different geometries using steps and ribs Measurements of heat transfer coefficients over the plate 	Experimental	<p>Ribs reduced heat transfer in the investigated range of variables</p> <p>Ribbed surfaces does not enhance heat transfer compared to the smooth plate</p> <p>Stepped plates (stairs) increases the heat transfer compared to the smooth plate case at all geometrical combinations based on projected length. A maximum increase of 23.21 % for a pitch to height ratio of 16:1 is obtained</p>	[Tanda, 2017] [Bhavvmani and Bergles, 1990]
<ul style="list-style-type: none"> Investigation of natural convection in wavy sinusoidal geometries (heat transfer) Measurements of heat transfer coefficients over the plate 	Experimental	<p>It is found that the wavy geometry transfers more heat based on projected area compared to the smooth plate case</p> <p>An increase of approximately 14-15 % is obtained based on a pitch to wavelength ratio of 0.3</p>	[Bhavvmani and Bergles, 1991]
<ul style="list-style-type: none"> An order of magnitude analysis for natural convective flows over vertical surfaces Both UWT and UWF boundary conditions are investigated 	Analytical	<p>The order of magnitude study successfully find an expression capable of obtaining the characteristics of natural convection from vertical surfaces for the entire Pr spectrum</p>	[Capobianchi and Aziz, 2012]
<ul style="list-style-type: none"> Numerical investigations of natural convection flows through corrugated channels Measurements of heat transfer coefficients over the plate 	Numerical	<p>A Nusselt number correlation is obtained for the fully developed flow as a function of Gr, Pr, L/W</p> <p>The results agree satisfactory with the analytical values for $\Theta = 0$ (vertical plate)</p>	[Faghri and Yutaka, 1986]
<ul style="list-style-type: none"> Laminar free convection from a vertical plate surface 	Analytical	<p>A correlation for Nu has been proposed including the limiting cases of zero and infinite Pr</p>	[Le Fevre 1956]

Field of investigation	Method	Findings	Reference
<ul style="list-style-type: none"> Correlating equations for both laminar and turbulent natural convection from vertical plates 	Literature review	Correlations for laminar cases for all ranges of Ra (= Pr Gr) have been developed, and recommendations are given as to which correlation should be used in a given regime. It is advised that a general correlation of the simple power law should not be used as it can not be justified due to poor agreement	[Churchill and Chu, 1975]
<ul style="list-style-type: none"> Comparison of thermal performance between plate-fin and pin-fin heat sinks in natural convection 	Analytical		
	Experiments	It has been found that the objective function affects which heat sink is better	Joo and Kim [2015]
	Optimization	Total heat dissipated objective function suggests that the plate-fin heat sink is better	
	Numerical CFD	Heat dissipation per unit mass suggests that the pin-fin heat sink is better	
<ul style="list-style-type: none"> Efficient 3D topology optimization of heat sinks in natural convection using the shape-dependent convection model on a circular plate-fin heat sink 	Numerical CFD	An optimized heat sink is found and investigated	Joo et al. [2018]
<ul style="list-style-type: none"> Natural convection flow along a vertical complex wavy surface with uniform heat flux 	Numerical Finite difference method	The temperature distribution is more sensitive to the amplitude of the first harmonic than the fundamental wave The wavy surface does not increase heat transfer compared to the flat plate case	Molla et al. [2007]

B | GCI calculations

The equations used for the evaluation of GCI are based on [Celik et al., 2008], and shown in Equation B.1-B.9.

$$\zeta = \left[\frac{1}{n} \sum_{i=1}^N (\Delta A_i) \right]^{1/2} \quad (\text{B.1})$$

Here the grid cell size is given by the summation of cell volumes, divided by the number of cells. The ratio between the grid cell sizes r , is given in equation B.2.

$$r = \frac{\zeta_{\text{coarse}}}{\zeta_{\text{fine}}} \quad (\text{B.2})$$

It is recommended that the grid refinement ratio is greater than 1.3. From here the apparent order p , of the numerical method used is approximated by Equation B.3 to B.5.

$$p_a = \frac{1}{\ln(r_{21})} \left| \ln \left| \frac{e_{32}}{e_{21}} \right| + \psi(p_a) \right| \quad (\text{B.3})$$

$$\psi(p_a) = \ln \left(\frac{r_{21}^{p_a} - S}{r_{32}^{p_a} - S} \right) \quad (\text{B.4})$$

$$S = 1 \cdot \text{sign} \left(\frac{e_{32}}{e_{21}} \right) \quad (\text{B.5})$$

Where the subscript 21 states the difference between the medium and fine mesh and 32 states the difference between the coarse and medium mesh according to $\zeta_1 < \zeta_2 < \zeta_3$. Furthermore, $e_{32} = \omega_3 - \omega_2$ and $e_{21} = \omega_2 - \omega_1$.

It should be noted that if either $e_{32} = \omega_3 - \omega_2$ or $e_{21} = \omega_2 - \omega_1$ is very close to zero, the above mentioned methods do not work. As ε approaches zero, it might indicate two things, namely that the exact solution has been obtained, or that the convergence is oscillatory. To ensure that the obtained values of ω is within the asymptotic range of convergence, the GCI is calculated for each grid refinement using Equation B.6 to B.7.

$$\text{GCI}_{21} = \frac{F_s e_{21}}{r_{21}^{p_a} - 1} \quad (\text{B.6})$$

$$\text{GCI}_{32} = \frac{F_s e_{32}}{r_{32}^{p_a} - 1} \quad (\text{B.7})$$

Where e_{21} and e_{32} describes the relative errors between the fine-medium and medium-coarse meshes respectively. The factor F_s is a factor of safety, which is set to 1.25 following .

When two GCI values are obtained it is possible to check whether the asymptotic range of convergence is reached by checking whether Equation B.8 is satisfied.

$$\frac{\text{GCI}_{32}}{r_{21}^{p_a} \text{GCI}_{21}} \approx 1 \quad (\text{B.8})$$

If Equation B.8 is satisfied, the mesh and numerical method used to calculate ω is independent and therefore valid as a solution method.

It is now possible to calculate the extrapolated value according to Equation B.9.

$$\omega_{\text{ext},21} = \frac{r_{21}^{p_a} \omega_1 - \omega_2}{r_{21}^{p_a} - 1} \quad (\text{B.9})$$

C | Python script used for mesh generation

```
1 import numpy as np
2 from matplotlib import pyplot as plt
3
4 def convert_np_to_str(np_array):
5     str_collection = []
6
7     for i in range(0, np_array.shape[0]):
8         np_str = "{0}".format(str(np_array[i]))
9         np_str = np_str.replace("[", "")
10        np_str = np_str.replace("]", "")
11        str_collection.append(np_str + "\n")
12
13    return str_collection
14
15
16 def insert_spline(lines, spline, idx):
17     beginning = lines[:idx]
18     end = lines[idx:]
19     beginning.extend(spline)
20     beginning.extend(end)
21
22     return beginning
23
24
25 def change_channel_width(lines, channel_width, channel_length,
26 channel_depth, bottom_length, out_in_fit):
27     lines[21] = "    ({0} 0 0)\n".format(out_in_fit)
28     lines[22] = "    ({0} 0 0)\n".format(channel_width+np.cos(phase_change
29 )*h)
30     lines[23] = "    ({0} {1} 0)\n".format(out_in_fit, channel_length)
31     lines[24] = "    ({0} {1} 0)\n".format(channel_width+np.cos(
32 phase_change)*h, channel_length)
33     lines[25] = "    ({0} 0 {1})\n".format(out_in_fit, channel_depth)
34     lines[26] = "    ({0} 0 {1})\n".format(channel_width+np.cos(
35 phase_change)*h, channel_depth)
36     lines[27] = "    ({0} {1} {2})\n".format(out_in_fit, channel_length,
37 channel_depth)
38     lines[28] = "    ({0} {1} {2})\n".format(channel_width+np.cos(
39 phase_change)*h, channel_length, channel_depth)
40     lines[29] = "    ({0} {1} 0)\n".format(out_in_fit, bottom_length)
41     lines[30] = "    ({0} {1} 0)\n".format(channel_width+np.cos(
42 phase_change)*h, bottom_length)
43     lines[31] = "    ({0} {1} {2})\n".format(out_in_fit, bottom_length,
44 channel_depth)
45     lines[32] = "    ({0} {1} {2})\n".format(channel_width+np.cos(
46 phase_change)*h, bottom_length, channel_depth)
47     lines[33] = "    ({0} {1} 0)\n".format(out_in_fit, channel_length-
```

```

bottom_length)
39 lines[34] = "      ({0} {1} 0)\n".format(channel_width+np.cos(
phase_change)*h, channel_length-bottom_length)
40 lines[35] = "      ({0} {1} {2})\n".format(out_in_fit, channel_length-
bottom_length, channel_depth)
41 lines[36] = "      ({0} {1} {2})\n".format(channel_width+np.cos(
phase_change)*h, channel_length-bottom_length, channel_depth)
42 return lines
43
44
45 def create_that_file(og_file_path, channel_width, channel_length,
channel_depth, bottom_length, out_in_fit, spline_01, spline_45,
spline_23, spline_67):
46 line_counter = 0
47
48 lines = None
49 with open(og_file_path + "blockMeshDict_template_movedoutlet.txt", "r"
) as file:
50     lines = file.readlines()
51
52 lines = change_channel_width(lines, channel_width, channel_length,
channel_depth, bottom_length, out_in_fit)
53
54 lines = insert_spline(lines, convert_np_to_str(spline_01), 83)
55 line_counter += len(spline_01)
56
57 lines = insert_spline(lines, convert_np_to_str(spline_45), 87 +
line_counter)
58 line_counter += len(spline_45)
59
60 lines = insert_spline(lines, convert_np_to_str(spline_23), 91 +
line_counter)
61 line_counter += len(spline_23)
62
63 lines = insert_spline(lines, convert_np_to_str(spline_67), 95 +
line_counter)
64
65 with open(og_file_path + "blockMeshDict", "w") as file:
66     file.writelines(lines)
67
68     return "success"
69
70 if __name__ == "__main__":
71
72     # directory path to where blockMeshDict_template.txt is located
73     dir_path = '/home/bjoern/Desktop/parameter_studie/20000/'
74
75     # =====
76     #These variables can be changed to alter the geometry of the channel.
77     L=0.1 #5/3 5/4 5/5 5/6 5/7
78     h=0.004 #0.008 0.006 0.004 0.002
79     phase_change = np.pi/1 #0 np.pi/2 np.pi/1
80     # =====

```

```

81
82 bottom_length = -0.05
83 channel_depth = 0.1
84 channel_length = 0.5
85 channel_width = 0.1
86 out_in_fit = h
87
88 y = np.arange(0,channel_length,L/40)
89
90 x = h*np.sin(((y+L/4) * np.pi )*(2/(L)))
91
92 x2 = h*np.sin((((y+L/4) * np.pi )*(2/(L)))+phase_change)
93 x3=x2+channel_width
94
95 a = [x, y]
96 b = [x3, y]
97 a2 = np.transpose(a)
98 b2 = np.transpose(b)
99 a3 = np.append(a2,np.zeros([len(a2),1]),1)
100 b3 = np.append(b2,np.zeros([len(b2),1]),1)
101 a4 = np.append(a2,np.full([len(a2),1],channel_depth),1)
102 b4 = np.append(b2,np.full([len(b2),1],channel_depth),1)
103
104 spline_01 = np.delete(a3, (0), axis=0)
105 spline_45 = np.delete(a4, (0), axis=0)
106 spline_23 = np.delete(b3, (0), axis=0)
107 spline_67 = np.delete(b4, (0), axis=0)
108
109 create_that_file(dir_path, channel_width, channel_length,
channel_depth, bottom_length, out_in_fit, spline_01, spline_45,
spline_23, spline_67)
110
111 # =====
112 #Plotting the channel
113 ax = plt.subplot(111)
114 ax.grid(True,which="both",ls="-")
115 ax.plot(x,y)
116 ax.plot(x3,y)
117 ax.axvline(x=0, color='black')
118 ax.axvline(x=0.1, color='black')
119 ax.axvline(x=h, color='green')
120 ax.axvline(x=(channel_width)+np.cos(phase_change)*h, color='green')
121 ax.set_xlim(-0.1,0.2)
122 ax.set_ylim(bottom_length,channel_length)
123 plt.show()
124 # =====
125 # =====
126 #Calculate the euclidean distance to compute length
127 #Increase the amount of points in y to obtain resonable results.
128 dx = x[1:]-x[:-1]
129 dy = y[1:]-y[:-1]
130
131 step_size = np.sqrt(dx**2+dy**2)

```

```
132
133     cumulative_distance = np.concatenate(([0], np.cumsum(step_size)))
134     dist=cumulative_distance[-1]
135 # =====
```

Listing C.1: Python script used to generate the necessary lines to fill the blockMeshDict template shown below.

```

1  /*-----* C++ *-----*\
2  | ===== |
3  |  \ \      /  F i e l d      | OpenFOAM: The Open Source CFD Toolbox |
4  |  \ \      /  O p e r a t i o n | Version: 5 |
5  |  \ \      /  A n d           | Web:      www.OpenFOAM.org |
6  |  \ \ /      M a n i p u l a t i o n | |
7  /*-----*/
8  FoamFile
9  {
10     version      2.0;
11     format        ascii;
12     class         dictionary;
13     object        blockMeshDict;
14 }
15 // * * * * * //
16
17 convertToMeters 1;
18
19 vertices
20 (
21     //block1
22     (0 0 0)//0
23     (4 0 0)//1
24     (0 5 0)//2
25     (4 5 0)//3
26     (0 0 0.1)//4
27     (4 0 0.1)//5
28     (0 5 0.1)//6
29     (4 5 0.1)//7
30     (0 0 0)//8
31     (4 0 0)//9
32     (0 5 0)//10
33     (4 5 0)//11
34     (0 0 0.1)//12
35     (4 0 0.1)//13
36     (0 5 0.1)//14
37     (4 5 0.1)//15
38
39
40 );
41
42 blocks
43 (
44     //block1
45     hex (0 1 3 2 4 5 7 6) (255 280 1) simpleGrading
46     (
47         (
48             (0.2 0.3 4) //20% x-dir, 30% cells, expansion = 4
49             (0.6 0.4 1) //60% x-dir, 40% cells, expansion = 1
50             (0.2 0.3 0.25) //20% x-dir, 30% cells, expansion = 0.25
51         )
52         1
53         1

```

```

54 )
55
56 //block1
57 hex (8 9 1 0 10 11 5 4) (255 28 1) simpleGrading
58 (
59   (
60     (0.2 0.3 4) //20% x-dir, 30% cells, expansion = 4
61     (0.6 0.4 1) //60% x-dir, 40% cells, expansion = 1
62     (0.2 0.3 0.25) //20% x-dir, 30% cells, expansion = 0.25
63   )
64   1
65   1
66 )
67 //block2
68 hex (2 3 13 12 6 7 15 14) (255 28 1) simpleGrading
69 (
70   (
71     (0.2 0.3 4) //20% x-dir, 30% cells, expansion = 4
72     (0.6 0.4 1) //60% x-dir, 40% cells, expansion = 1
73     (0.2 0.3 0.25) //20% x-dir, 30% cells, expansion = 0.25
74   )
75   1
76   1
77 )
78 );
79
80 edges
81 (
82   spline 0 2
83   (
84   )
85
86   spline 4 6
87   (
88   )
89
90   spline 1 3
91   (
92   )
93
94   spline 5 7
95   (
96   )
97 );
98
99 boundary
100 (
101   inlet
102   {
103     type patch;
104     faces
105     (
106       (8 10 11 9)

```

```
107     );
108 }
109 outlet
110 {
111     type patch;
112     faces
113     (
114         //Hvis block1
115         (12 13 14 15)
116     );
117 }
118 heatedWall_right
119 {
120     type wall;
121     faces
122     (
123         //block1
124         (7 3 1 5)
125     );
126 };
127 }
128
129 heatedWall_left
130 {
131     type wall;
132     faces
133     (
134         //block1
135         (2 6 4 0)
136     );
137 }
138
139 adiWallbot
140 {
141     type wall;
142     faces
143     (
144         //block1
145         (8 0 4 10)
146         (9 11 5 1)
147         (2 12 14 6)
148         (15 13 3 7)
149     );
150 }
151
152 frontAndBack
153 {
154     type empty;
155     faces
156     (
157         //fronts
158         (0 1 3 2)//0
159         (8 9 1 0)//1
```

```
160         (2 3 13 12)//2
161         //backs
162         (4 6 7 5)//0
163         (10 4 5 11)//1
164         (14 15 7 6)//2
165
166
167     );
168 }
169 );
170
171 // mergePatchPairs
172 // (
173 // );
174
175 // ***** //
```

Listing C.2: blockMeshDict template

Bibliography

- Abidi-Saad et al., 2016.** Aissa Abidi-Saad, Guillaume Polidori, Mahfoud Kadja, Fabien Beaumont, Catalin-Viorel Popa and Abdelkader Korichi. *Experimental investigation of natural convection in a vertical rib-roughened channel with asymmetric heating*. Mechanics Research Communications, 76, 1 – 10, 2016. ISSN 0093-6413. doi: <https://doi.org/10.1016/j.mechrescom.2016.06.001>.
- Acharya and Mehrotra, 1993.** S. Acharya and A. Mehrotra. *Natural convection heat transfer in smooth and ribbed vertical channels*. International Journal of Heat and Mass Transfer, 36(1), 236 – 241, 1993. ISSN 0017-9310. doi: [https://doi.org/10.1016/0017-9310\(93\)80085-9](https://doi.org/10.1016/0017-9310(93)80085-9).
- Altun and Ziylan, 2019.** Aziz Hakan Altun and Orkun Ziylan. *Experimental investigation of the effects of horizontally oriented vertical sinusoidal wavy fins on heat transfer performance in case of natural convection*. International Journal of Heat and Mass Transfer, 139, 425 – 431, 2019. ISSN 0017-9310. doi: <https://doi.org/10.1016/j.ijheatmasstransfer.2019.05.009>.
- Ambrosini and Tanda, dec 2005.** Dario Ambrosini and Giovanni Tanda. *Comparative measurements of natural convection heat transfer in channels by holographic interferometry and schlieren*. European Journal of Physics, 27(1), 159–172, 2005. doi: 10.1088/0143-0807/27/1/016.
- Aydin, 1997.** Murat Aydin. *Dependence of the natural convection over a vertical flat plate in the presence of the ribs*. International Communications in Heat and Mass Transfer, 24(4), 521 – 531, 1997. ISSN 0735-1933. doi: [https://doi.org/10.1016/S0735-1933\(97\)00037-7](https://doi.org/10.1016/S0735-1933(97)00037-7).
- Bar-Cohen and Rohsenow, 02 1984.** A. Bar-Cohen and W. M. Rohsenow. *Thermally Optimum Spacing of Vertical, Natural Convection Cooled, Parallel Plates*. Journal of Heat Transfer, 106(1), 116–123, 1984. ISSN 0022-1481. doi: 10.1115/1.3246622. URL <https://doi.org/10.1115/1.3246622>.
- Bhavnani and Bergles, 1991.** S. H. Bhavnani and A. E. Bergles. *Natural convection heat transfer from sinusoidal wavy surfaces*. Wärme - und Stoffübertragung, 26, 341–349, 1991. URL <https://link-springer-com.zorac.aub.aau.dk/article/10.1007/BF01591667#citeas>.
- Bhavnani and Bergles, 1990.** Sushil H. Bhavnani and Arthur E. Bergles. *Effect of surface geometry and orientation on laminar natural convection heat transfer from a vertical flat plate with transverse roughness elements*. International Journal of Heat and Mass Transfer, 33(5), 965 – 981, 1990. ISSN 0017-9310. doi: [https://doi.org/10.1016/0017-9310\(90\)90078-9](https://doi.org/10.1016/0017-9310(90)90078-9).

- Capobianchi and Aziz, 2012.** M. Capobianchi and A. Aziz. *A scale analysis for natural convective flows over vertical surfaces*. International Journal of Thermal Sciences, 54, 82 – 88, 2012. ISSN 1290-0729. doi: <https://doi.org/10.1016/j.ijthermalsci.2011.11.009>.
- Celik et al., 07 2008.** Ismail B. Celik, Urmila Ghia, Patrick J. Roache, Christopher J. Freitas, Hugh Coleman and Peter E. Raad. *Procedure for Estimation and Reporting of Uncertainty Due to Discretization in CFD Applications*. Journal of Fluids Engineering, 130(7), 2008. ISSN 0098-2202. doi: 10.1115/1.2960953.
- Cengel, 2003.** Y. A. Cengel. *Heat Transfer A Practical Approach*. McGraw Hill, 2 edition, 2003. ISBN 978-0072458930.
- Churchill and Chu, 1975.** Stuart W. Churchill and Humbert H.S. Chu. *Correlating equations for laminar and turbulent free convection from a vertical plate*. International Journal of Heat and Mass Transfer, 18(11), 1323 – 1329, 1975. ISSN 0017-9310. doi: [https://doi.org/10.1016/0017-9310\(75\)90243-4](https://doi.org/10.1016/0017-9310(75)90243-4).
- Desrayaud and Fichera, 2002.** Gilles Desrayaud and Alberto Fichera. *Laminar natural convection in a vertical isothermal channel with symmetric surface-mounted rectangular ribs*. International Journal of Heat and Fluid Flow, 23(4), 519 – 529, 2002. ISSN 0142-727X. doi: [https://doi.org/10.1016/S0142-727X\(02\)00136-4](https://doi.org/10.1016/S0142-727X(02)00136-4).
- Faghri and Yutaka, 1986.** M. Faghri and Asako Yutaka. *Periodic, fully developed, natural convection in a channel with corrugated confining walls*. International Journal of Heat and Mass Transfer, 29(12), 1931 – 1936, 1986. ISSN 0017-9310. doi: [https://doi.org/10.1016/0017-9310\(86\)90011-6](https://doi.org/10.1016/0017-9310(86)90011-6).
- Ghosh Moulic and Yao, 11 1989.** S. Ghosh Moulic and L. S. Yao. *Mixed Convection Along a Wavy Surface*. Journal of Heat Transfer, 111(4), 974–979, 1989. ISSN 0022-1481. doi: 10.1115/1.3250813.
- Joo and Kim, 2015.** Younghwan Joo and Sung Jin Kim. *Comparison of thermal performance between plate-fin and pin-fin heat sinks in natural convection*. International Journal of Heat and Mass Transfer, 83, 345 – 356, 2015. ISSN 0017-9310. doi: <https://doi.org/10.1016/j.ijheatmasstransfer.2014.12.023>. URL <http://www.sciencedirect.com/science/article/pii/S0017931014011132>.
- Joo et al., 2018.** Younghwan Joo, Ikjin Lee and Sung Jin Kim. *Efficient three-dimensional topology optimization of heat sinks in natural convection using the shape-dependent convection model*. International Journal of Heat and Mass Transfer, 127, 32 – 40, 2018. ISSN 0017-9310. doi: <https://doi.org/10.1016/j.ijheatmasstransfer.2018.08.009>. URL <http://www.sciencedirect.com/science/article/pii/S0017931018331764>.

- Joshi et al., 06 1989.** Y. Joshi, T. Willson and III Hazard, S. J. *An Experimental Study of Natural Convection From an Array of Heated Protrusions on a Vertical Surface in Water*. Journal of Electronic Packaging, 111(2), 121–128, 1989. ISSN 1043-7398. doi: 10.1115/1.3226516.
- Kraus and Bar-Cohen, 1983.** Allan D. Kraus and Avram Bar-Cohen. *Thermal Analysis and Control of Electronic Equipment*. McGraw-Hill, 1 edition, 1983. ISBN 978-0070354166.
- Le Fevre, 1956.** E.J. Le Fevre. *Laminar free convection from a vertical plane surface*. International Congress for Applied Mechanics, 4, 168–174, 1956.
- Minocha et al., 2016.** Nitin Minocha, Jyeshtharaj B. Joshi, Arun K. Nayak and Pallippattu K. Vijayan. *3D CFD simulations to study the effect of inclination of condenser tube on natural convection and thermal stratification in a passive decay heat removal system*. Nuclear Engineering and Design, 305, 582 – 603, 2016. ISSN 0029-5493. doi: <https://doi.org/10.1016/j.nucengdes.2016.06.020>.
- Mishra, 2004.** Rajeev Mishra. *The Temperature Ratings Of Electronic Parts*. <https://www.electronics-cooling.com/2004/02/the-temperature-ratings-of-electronic-parts/>, 2004. Downloaded: 22-04-2020.
- Molla et al., 04 2007.** Mamun Molla, Anwar Hossain and Lun-Shin Yao. *Natural-Convection Flow Along a Vertical Complex Wavy Surface With Uniform Heat Flux*. Journal of Heat Transfer, 129(10), 1403–1407, 2007. ISSN 0022-1481. doi: 10.1115/1.2755062. URL <https://doi.org/10.1115/1.2755062>.
- Ostrach, 1952.** Simon Ostrach. *An analysis of laminar free-convection flow and heat transfer about a flat plate paralalled to the direction of the generating body force*. <https://ntrs.nasa.gov/search.jsp?R=19930092147>, 1952. Downloaded: 23-03-2020.
- Pankaj et al., 2018.** Shitole Pankaj, Bhosle Santosh, Kulkarni Kishor and Joshi Sarang. *Experimental Investigation of Heat Transfer by Natural Convection with Perforated Pin Fin Array*. Procedia Manufacturing, 20, 311 – 317, 2018. ISSN 2351-9789. doi: <https://doi.org/10.1016/j.promfg.2018.02.046>.
- Roy et al., 2019.** Krishna Roy, Asis Giri and Biplab Das. *A computational study on natural convection heat transfer from an inclined plate finned channel*. Applied Thermal Engineering, 159, 113941, 2019. ISSN 1359-4311. doi: <https://doi.org/10.1016/j.applthermaleng.2019.113941>.
- Saha and Chanda, 2019.** Arun K. Saha and Sourayon Chanda. *Fully-developed natural convection in a periodic array of pin-fins*. International Journal of Thermal Sciences, 137, 325 – 336, 2019. ISSN 1290-0729. doi: <https://doi.org/10.1016/j.ijthermalsci.2018.11.020>.

- Sakanova and Tseng, 2018.** Assel Sakanova and King Jet Tseng. *Comparison of pin-fin and finned shape heat sink for power electronics in future aircraft*. Applied Thermal Engineering, 136, 364 – 374, 2018. ISSN 1359-4311. doi: <https://doi.org/10.1016/j.applthermaleng.2018.03.020>.
- Stimpson et al., 2007.** C. J. Stimpson, C. D. Ernst, P. Knupp, P. P. Pebay and D. Thompson. *The Verdict Library Reference Manual*, 2007. URL <https://pdfs.semanticscholar.org/8909/f7ef51980d03ebab251251bde877eba92a06.pdf>.
- Talukdar et al., 2019.** Deboprasad Talukdar, Chung-Gang Li and Makoto Tsubokura. *Numerical investigation of laminar compressible natural convection flow in asymmetrically and isothermally heated open-ended inclined channel*. International Journal of Heat and Mass Transfer, 130, 83 – 97, 2019. ISSN 0017-9310. doi: <https://doi.org/10.1016/j.ijheatmasstransfer.2018.10.076>.
- Tanda, 1997.** Giovanni Tanda. *Natural convection heat transfer in vertical channels with and without transverse square ribs*. International Journal of Heat and Mass Transfer, 40(9), 2173 – 2185, 1997. ISSN 0017-9310. doi: [https://doi.org/10.1016/S0017-9310\(96\)00246-3](https://doi.org/10.1016/S0017-9310(96)00246-3).
- Tanda, 2008.** Giovanni Tanda. *Natural convective heat transfer in vertical channels with low-thermal-conductivity ribs*. International Journal of Heat and Fluid Flow, 29(5), 1319 – 1325, 2008. ISSN 0142-727X. doi: <https://doi.org/10.1016/j.ijheatfluidflow.2008.05.004>.
- Tanda, 2017.** Giovanni Tanda. *Experiments on natural convection in water-cooled ribbed channels with different aspect ratios*. International Journal of Heat and Mass Transfer, 110, 606 – 612, 2017. ISSN 0017-9310. doi: <https://doi.org/10.1016/j.ijheatmasstransfer.2017.03.050>.
- Wang and Vanka, 1995.** G. Wang and S.P. Vanka. *Convective heat transfer in periodic wavy passages*. International Journal of Heat and Mass Transfer, 38(17), 3219 – 3230, 1995. ISSN 0017-9310. doi: [https://doi.org/10.1016/0017-9310\(95\)00051-A](https://doi.org/10.1016/0017-9310(95)00051-A).
- Zografos and Sunderland, 1990.** Antonios I. Zografos and J. Edward Sunderland. *Natural convection from pin fin arrays*. Experimental Thermal and Fluid Science, 3(4), 440 – 449, 1990. ISSN 0894-1777. doi: [https://doi.org/10.1016/0894-1777\(90\)90042-6](https://doi.org/10.1016/0894-1777(90)90042-6).